LA-UR-22-20081
Accepted Manuscript

Ce post-treatment for increased corrosion resistance of AA2024-T3 anodized in tartaric-sulfuric acid

Ramirez, Oscar M. P.
Tunes, Matheus Araujo
Mennucci, Marina M.
Starykevich, Maksim
Neves, Cristina
Ferreira, Mario G. S.
Pogatscher, Stefan
de Melo, Hercilio G.

Provided by the author(s) and the Los Alamos National Laboratory (2022-05-16).

To be published in: Corrosion Science

DOI to publisher's version: 10.1016/j.corsci.2022.110371

Permalink to record:
http://permalink.lanl.gov/object/view?what=info:lanl-repo/lareport/LA-UR-22-20081

Journal Pre-proof

Ce post-treatment for increased corrosion resistance of AA2024-T3 anodized in tartaric-sulfuric acid

Oscar Mauricio Prada Ramirez, Matheus Araujo Tunes, Marina Martins Mennucci, Maksim Starykevich, Cristina Neves, Mário G.S. Ferreira, Stefan Pogatscher, Hercílio Gomes De Melo

PII: S0010-938X(22)00289-X

DOI: https://doi.org/10.1016/j.corsci.2022.110371

Reference: CS110371

To appear in: *Corrosion Science*

Received date: 29 January 2022
Revised date: 11 April 2022
Accepted date: 9 May 2022

Please cite this article as: Oscar Mauricio Prada Ramirez, Matheus Araujo Tunes, Marina Martins Mennucci, Maksim Starykevich, Cristina Neves, Mário G.S. Ferreira, Stefan Pogatscher and Hercílio Gomes De Melo, Ce post-treatment for increased corrosion resistance of AA2024-T3 anodized in tartaric-sulfuric acid, *Corrosion Science,* (2022) doi:https://doi.org/10.1016/j.corsci.2022.110371

Ce post-treatment for increased corrosion resistance of AA2024-T3 anodized in tartaric-sulfuric acid

OSCAR MAURICIO PRADA RAMIREZ[1], MATHEUS ARAUJO TUNES[2], MARINA MARTINS MENNUCCI[3], MAKSIM STARYKEVICH[3], CRISTINA NEVES[3], MÁRIO G. S. FERREIRA[3], STEFAN POGATSCHER[4], HERCÍLIO GOMES DE MELO[1]

[1]Escola Politécnica da Universidade de São Paulo, Av. Prof. Mello de Moraes, 2463, São Paulo – SP – Brazil.
[2]Materials Science and Technology Division, Los Alamos National Laboratory, Los Alamos 87545, New Mexico, USA.
[3]CICECO-Aveiro Institute of Materials, Department of Materials and Ceramic Engineering, University of Aveiro, 3810-193 Aveiro, Portugal.
[4]Chair of Non-Ferrous Metallurgy, Montanuniversitaet Leoben, 18 Franz-Josef-Strasse, 8700, Leoben, Austria.

Abstract

The effect of a post-treatment for short time in 50 mM $Ce(NO_3)_3$ solution, with or without H_2O_2, on the corrosion of AA2024-T3 anodized in tartaric-sulfuric acid was investigated. Electrochemical (EIS, polarization curves) and corrosion (immersion) tests showed improved performance for samples post-treated at 50 ^{o}C in the H_2O_2 containing solution. Microstructural characterization (SEM, STEM, GDOES) evidenced the presence of Ce oxyhydroxides both at the surface and within the pores of the anodized layer, and their preferential interaction with defective sites both at micro and nanoscale. Important amounts of Ce-species were found near corrosion products, indicating active corrosion protection by Ce ions.

Keywords: Anodization, Aluminium Alloy, Electrochemical Impedance Spectroscopy, Scanning Transmission Electron Microscopy, Ce nanoparticles.

1. Introduction

The modification of materials through the action of external physicochemical forces – such as corrosion – is nowadays responsible for economic impact and losses in the order of 300 billion dollars only in the United States[1]. Thus, the development of new corrosion-resistant materials and better corrosion-related technical methodologies are of mandatory importance to achieve higher levels of materials' sustainability in a wide variety of fields ranging from the aerospace industry to functional materials applied in the energy sector. The desirable mechanical properties, high tensile strength and low density, of aluminium alloy 2024-T3 (AA2024-T3) makes it a material of first choice in the aerospace industry [2]. The good mechanical properties result from a complex microstructure, comprising a range of dispersoids and strengthening particles [3,4], achieved by means of alloying elements addition, such as Mg, Mn and Cu, and thermomechanical treatments carried out during the production of the alloy [5]. However, during the solidification process, alloying elements and impurities also segregate and precipitate as large (typically few tenths up to more than 10 micrometres) intermetallic particles (IM) [5], severely hindering local corrosion resistance of the alloy, as they frequently exhibit different electrochemical potential compared to the matrix, thus, enhancing local galvanic activity [5–10]. Moreover, IMs are often found in colonies constituted of particles, either of the same or of different types, providing ideal sites for pitting and intergranular corrosion initiation and propagation [5]. Therefore, to achieve the levels of protection required in the aerospace industry AA2024-T3 needs an efficient corrosion protection system [11,12].

In the aeronautical industry, anodizing is frequently used to protect Al alloys from corrosion. The procedure is performed in acidic electrolyte and results in an oxide layer exhibiting a duplex structure composed of a thick porous layer and a thin barrier layer [13,14]. The former layer provides the basis for adhesion of protective organic coatings, whereas the latter enhances the corrosion protection [15]. When clad or commercially pure Al is used as substrate for anodizing, the oxide layer presents a regular columnar structure [11,16–19]. However, the oxide structure changes dramatically when the microstructure of the Al alloy is more complex, as in the case of alloys of the 2XXX series. For these materials, it is claimed that both the incorporation of Cu particles into the anodic oxide layer during its growth, activating O_2 generation [20], and the differences in the oxidation rates of the matrix and the IMs [21] produce defective structures [22–25]. However, in an aircraft, independent of the substrate, the oxide layer is further protected to guarantee reliable corrosion protection.

Chromic acid anodizing (CAA) is the standard procedure in the aerospace industry. Following CAA, the piece is generally post-treated by immersion in Alodine (Henkel Alodine®), a commercial post-treatment mainly containing Cr(VI) and F^- species [26], and protected with a primer containing strontium chromate ($SrCrO_4$) as corrosion inhibitor [27]. The extensive use of surface treatments with chromates to protect metallic substrates against corrosion is justified by their low cost and by the fact that, besides providing efficient corrosion protection, chromate ions exhibit self-healing abilities [28–30]. Although consolidated and efficient as a methodology for corrosion protection, chromate-based surface treatments are aggressive for the environment and for the human health; however, although already prohibited in various industrial fields, their application in the aerospace industry is still allowed, due to safety requirements [31,32]. Nevertheless, considerable efforts have been made by industries and scientists to find a suitable substitute for chromates in the Al surface treatment industry, as can be verified by numerous works published in the literature. Several anodizing procedures employing alternative electrolytes are already being used in commercial aviation, like boric and sulfuric acid by Boeing [33], tartaric-sulfuric acid (TSA) by Airbus [34], and phosphoric and sulfuric acid that is intended to be used by Fokker [35]. In the present work, we have employed TSA, which, in addition to its environmental friendliness, produces anodic oxide layers with corrosion protection performance similar to those produced with CAA [26].

Rare earth salts, particularly Ce salts, have been used to inhibit corrosion of Al alloys [36–41]. In the previous works carried out by Hinton and co-workers [42,43], it has been shown that the addition of a few hundred ppm of cerium salts to a NaCl solution caused the formation of a conversion layer composed of Ce(III) Ce(IV) oxides, and hydroxides, significantly reducing the corrosion rate. However, in these initial works, the formation and thickening of the oxide layer resulting from the aqueous solution occurred very slowly and could take several days [43,44]. Several later works have shown that the addition of H_2O_2 to an aqueous solution containing Ce salts reduced the treatment time to just a few minutes, creating a relatively thick conversion layer on the aluminium alloy surface [36,37,40,45,46]. Mechanisms available in the literature propose that the addition of H_2O_2 accelerates the oxidation of Ce^{3+} to Ce^{4+}, which then precipitates as Ce oxides and hydroxides at cathodic sites due to increased pH [45,47,48], thus hindering electrochemical activity.

Post-treatments based on Ce ions have also been used to protect anodized Al alloys [16,47,49–52]. In this sense, Saeedikhani et al. [49] studied the effect of the addition of cerium sulphate to the anodizing bath (sulfuric/boric/phosphoric acid) for the AA2024-T3, they concluded that the presence of Ce ions leads to increased homogeneity of the anodic layer and a greater thickness of the barrier layer, improving the corrosion resistance of the anodized substrate. Another strategy, is to use Ce salts in a post-anodizing treatment step aiming to produce a cerium oxide layer on top of the anodic oxide film [29,47,50]. Gordovskaya et al. [47] produced Ce oxide layers on pure Al and AA7075 previously anodized either in sulfuric acid or in tartaric-sulfuric acid (TSA) bath, by immersion in a solution containing cerium nitrate and hydrogen peroxide. Their results showed the development of a Ce oxide layer with about 50-100 nm on top of the anodized substrates resulting in a significant improvement in the corrosion resistance, evaluated by means of immersion tests in NaCl containing solution; the authors also report that adding tartaric acid to the anodizing bath entails the precipitation of Ce-oxide within the pores of the anodized layer resulting in a thicker, more uniform and corrosion resistant cerium layer [47]; however, the TEM images displayed in the paper indicate the blockage of the pore openings, which must be a consequence of the relatively long post-treatment time (30 min). Carangelo et al. [29] used a similar Ce post-treatment to that employed by Gordovskaya et al. [47] to seal an AA2024-T3 anodized in TSA, and used EIS to compare the behaviour with hot water and sodium chromate sealing, all sealing procedures performed during 30 minutes. They confirmed the deposition of Ce-oxide on top of the porous oxide layer and reported improved

EIS performance of the Ce-sealed sample after short immersion time in sulphate solution when compared with the other two sealing procedures [29]. By fitting the EIS diagrams acquired during the sealing procedure with electrical equivalent circuits, they reported an increase in the capacity of the barrier layer during sealing in the sodium chromate solution, not verified during Ce-based or boiling water sealing, and concluded that sodium chromate post-treatment heavily attacks the porous oxide structure associated with a thinning of the barrier layer [29]. Complementing their previous work [29], Carangelo et al. [50], by means of EIS and immersion tests in 3.5% NaCl solution, showed a best corrosion behaviour of the Ce-sealed samples compared to the chromate and hot water sealing. In another work, Terada et al. [51] reported that the addition of Ce ions to the hydrothermal sealing bath increased the corrosion resistance of AA2024-T3 anodized in TSA and then coated with an hybrid sol-gel coating.

In two previous works, Prada-Ramirez et al. [16,52] investigated the use of a post-treatment step in solutions containing $Ce(NO_3)_3.6H_2O_2$ to improve the corrosion resistance of clad AA2024-T3 anodized in TSA. The effects of Ce concentration, temperature, immersion time as well as the addition of H_2O_2 were studied. In accordance with results reported in the literature for Ce conversion layers applied to bare (non-anodized) Al alloys [36,37,40,45,46], it was found that adding H_2O_2 to the Ce solution enhanced the precipitation of Ce-oxyhydroxides [16] , thus beneficial effects were also verified by moderate heating, up to 50 ^oC, the Ce containing solution. Conversely, in these previous investigations, as the anodic oxide layer obtained from the clad substrate was quite homogeneous, the precipitation of Ce containing compounds was not intensively observed on the samples surface, even though S/TEM analysis have showed precipitation of Ce-rich nanoparticles within the pores of the anodized layer [16]. In the present investigation, the most promising conditions identified in these two previous works [16,52] were used as a post-treatment step to improve the corrosion resistance of the more microstructurally complex AA2024-T3 anodized in TSA. In this present research, the main focus is to investigate the corrosion resistance and the distribution of Ce species in the anodized layer, as well as their interaction with regions with intermetallic inclusions of the anodized substrate. As opposed to the previous works of Gordovskaya et al. [47] and Carangelo et al. [29,50] the post-treatment was applied for a short period, 2 min, aiming to keep the pores mouth open for subsequent application of a primer layer, a step already under investigation.

2. Experimental

2.1. Samples preparation

AA2024-T3 sheets with nominal composition (in wt. %) 3.8-4.9 Cu, 1.2-1.8 Mg, 0.3-0.9 Mn, 0.5 Fe, 0.5 Si, 0.25 Zn, 0.15 Ti, 0.1 Cr and balance of Al were used as substrate [53]. The sheets were cut as samples with (6 x 4 x 0.105) cm and cleaned by sonification in acetone for 10 minutes. Surface pre-treatment consisted in dipping the samples in an alkaline etching solution (40 $g.L^{-1}$ NaOH) at 40 °C for 30 s, followed by their immersion in a chromate-free commercial acid dismutting bath (Turco Smuttgo) at room temperature for 15 s. Abundant washing with deionized water was used after the end of each step of the procedure.

2.2. Anodizing procedure

TSA anodizing (40 g.L^{-1} H_2SO_4 + 80 g.L^{-1} $C_4H_6O_6$) was carried out at a constant voltage of 14 V for 20 minutes and at a controlled temperature of 37±2 °C [11,16,52,54]. Then, after rinsing with deionized water, the samples were post treated for 2 min under the following conditions: 50 mM $Ce(NO_3)_3.6H_2O$ at 50°C (Ce 50C); 50 mM $Ce(NO_3)_3.6H_2O$ + H_2O_2 (10% v/v) at 25°C (CeP 25C) or at 50°C (CeP 50C). Non-post treated samples, named unsealed (UNS), were used as control. Table 1 summarizes the experimental conditions and presents the acronyms that will be used hereafter.

Table 1. Applied post-treatments and their acronyms.

Condition / Acronyms	$Ce(NO_3)_3.6H_2O$ mM	H_2O_2 % v/v	Temperature °C	Time min
UNS	-	-	-	-
Ce 50C	50	-	50	2
CeP 25C	50	10	25	2
CeP 50C	50	10	50	2

2.3. Corrosion behaviour

Potentiodynamic polarization curves and electrochemical impedance spectroscopy (EIS) in 0.1 mol L^{-1} NaCl solution were used to evaluate the corrosion behaviour of the different samples. A three-electrode cell consisting of the anodized piece (3.14 cm^2 of exposed area), an Ag/AgCl (KCl satd) reference and a platinum sheet counter electrode was employed. The experiments were carried out with a Potentiostat/Galvanostat/ZRA (Gamry reference 600+).

Potentiodynamic polarization curves were acquired after 4h stabilization of the open circuit potential (OCP) in a range from -0.5 V to +1.0 V vs. OCP with scan rate of 1 mVs^{-1}. For the EIS tests the AC signal perturbation amplitude was 10 mV (rms) in the frequency range from 10^5 Hz to 10^{-2} Hz. Seven points were acquired for each frequency decade. For all samples, the EIS experiments were terminated at 168 h (1 week) when corrosion zones were visible in the surface of the samples with best performance. To check for reproducibility, all experiments were carried out at least in triplicate. Electric equivalent circuits (EEC) (Zview®) were employed to fit the EIS diagrams.

2.4. Microstructural Characterization

Microstructural characterization of the samples (surface and cross-section) was done using a scanning electron microscopy (SEM) with a field emission gun FE-SEM-Inspect 50, equipped with facilities for energy dispersive X-ray analysis (EDX). As-prepared and corroded (after the end of the EIS experiments) samples were analysed, which were also observed by optical microscopy (ZEISS reference Stemi 2000-C stereomicroscope).

Lamellae for Scanning Transmission Electron Microscopy (STEM) were prepared using a conventional Focused Ion Beam (FIB) to obtain electron-transparent samples [55]. To protect the anodic layer from possible FIB-induced damage, a 2 μm thick Pt layer was deposited onto the top of the sample prior the milling and trenching stages. Further details on both sample preparation method and electron-microscopy for analysing these samples in the STEM are given in a previous publication by our group [16]. Imaging and EDX maps were acquired.

Atomic Force Microscopy (AFM) was employed to evaluate samples roughness. Measurements were carried out with a Veeco Multimode IV atomic force microscope, equipped with a j-type scanner (100×100×5 μm scan range), having a resolution limit/detection 1 nm (XY direction) and 0.1 nm (Z direction) [56,57] and were performed in tapping mode, with silicon probes operating at a resonance frequency of about 320 kHz and a force constant of 42 N/m. The analysis of the images was carried out with the Gwiddeon software (version 2.37).

2.5. Glow Discharge Optical Emission Spectroscopy (GDOES)

Depth profiles of the anodized layers without and with Ce post-treatment were acquired by GDOES. The depth profile analysis was carried out with a HORIBA GDProfiler 2. Argon sputtering of the sample surface was performed at a pressure of 650 Pa and power of 30 W. The measurements were stopped when the erosion reached the substrate. The thickness of the anodic oxide layer as well as the Ce distribution within the pores were evaluated with this technique.

3. Results and discussion

3.1 Microstructural characterization

Figure 1 shows a SEM image and the corresponding EDX maps of the AA2024-T3 surface showing the distribution and chemical composition of the IMs. The average area of these particles was around 1.89±0.17 μm^2, indicating the predominance of small-sized IMs, and the area fraction occupied by them was about 2.45±0.29 %, consistent with the results reported by Queiroz et al. [9] for the same alloy, but slightly lower than the 2.83% determined by Boag et al. [3]. Two main types of IMs were identified: one containing Cu and Mg (possibly S-phase Al_2CuMg) and the other containing Cu, Fe and Mn, in accordance with the composition of the IMs of the AA2024-T3 reported in the literature [3,4,9,54]. Si-rich IMs were seldom identified in the studied alloy. The presence of these particles disturb the regular growth of the oxide layer, introducing defective regions and reducing the overall corrosion resistance of the anodized sample [13,14,21,58].

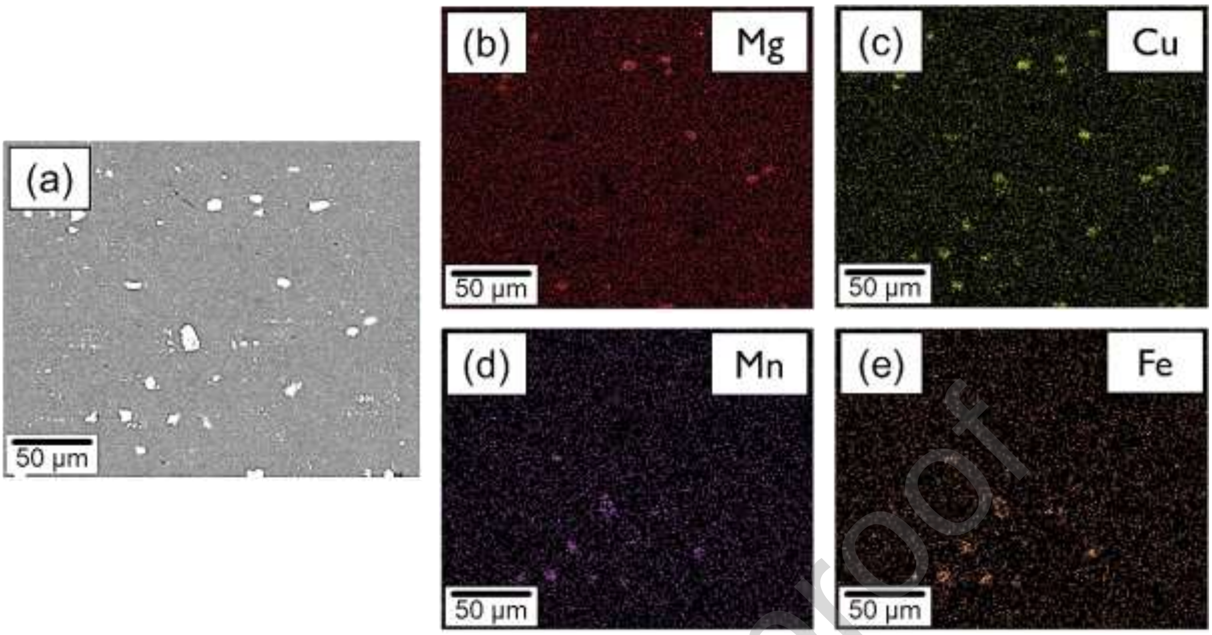

Figure 1. SEM and EDX maps of the AA2024-T3.

Surface and cross-section SEM images of the anodic layer are presented in Figure 2. The top surface exhibits a large number of defective sites (Figure 2(a)), possibly related to the presence of IMs in the base metal which have been totally or partially dissolved during the anodizing treatment [20,26,59–61]. The oxide thickness is in the range of (2.9 ± 0.2) μm (Figure 2(b)), well in accordance with results previously published in the literature for TSA anodized Al alloys [12,59,62], but thinner than that reported for a clad alloy anodized under the same condition [52], indicating enhanced dissolution of the anodized layer formed on the AA2024-T3 substrate during its growth. A cavity in the cross section of the oxide layer is depicted in Figure 2(c), the EDX analysis of the marked area evidences the presence of Al, Cu and Mg (Figure 2(d)), and its dimensions are typical of the larger IMs found in the alloy microstructure, indicating that it may have originated due to partial/incomplete oxidation during the anodizing process. The cavity is surrounded by the anodic oxide, suggesting that the particle oxidation may have occurred during the early stage of anodizing; however, the formed oxide layer is thinner and defective, as shown by the cracks in the peripheral region (indicated with arrows in (c)). The occluded geometry of such defect may constitute a preferential site for electrolyte stagnation and aggressive species accumulation impairing the corrosion protection of the anodized alloy; furthermore, the morphology of the oxide in this region is cracked and thinner, which can further increase the susceptibility to local attack.

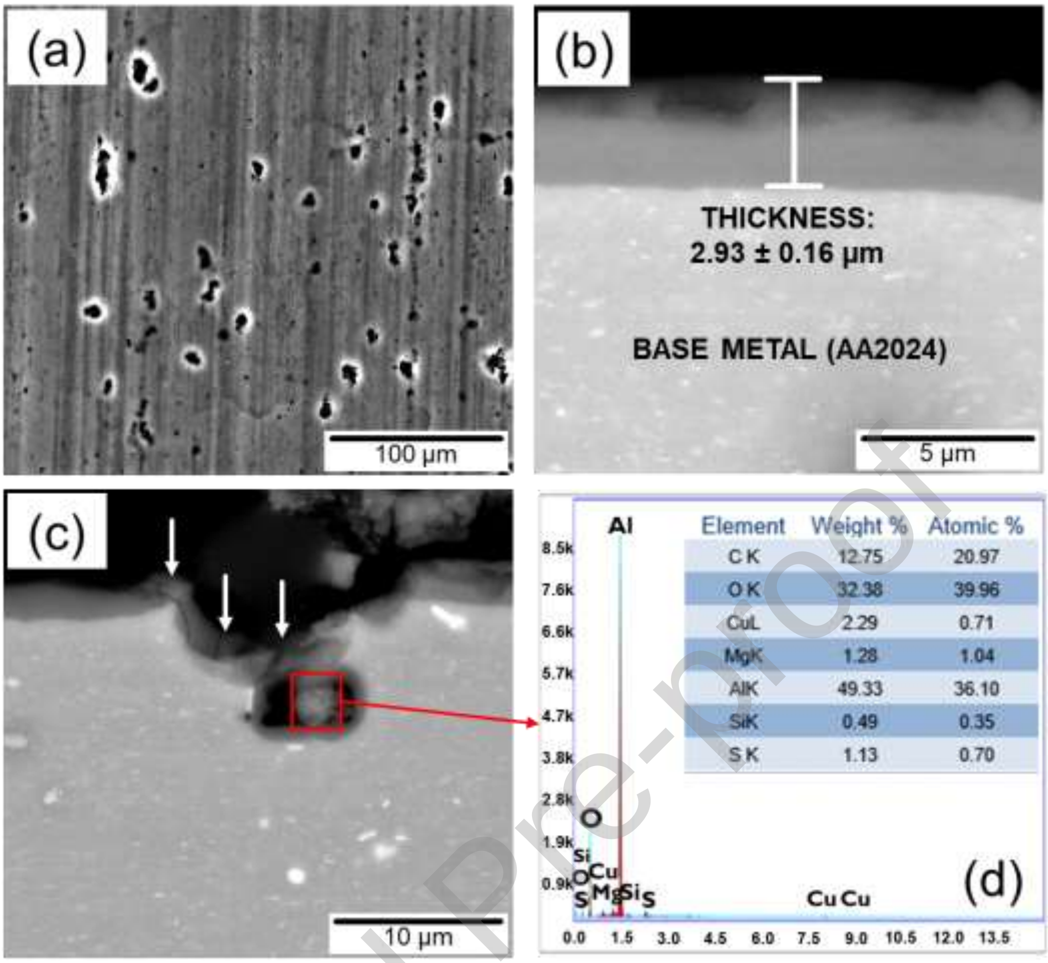

Figure 2. SEM-EDX characterization of the AA2024-T3 anodized in TSA: (a) top surface, (b) cross-section thickness, (c) cross-section cavity, (d) EDX analysis performed in the defective region. Cracks in the anodic oxide layer are indicated by white arrows in (c),

Figure 3 displays photographs of the surfaces of the anodized samples after the different post-treatments. Clearly, only the sample CeP 50C (Figure 3(d)) exhibits a significant superficial difference, presenting a homogeneous yellow coloration, whereas the other samples showed a homogeneous grey surface. This indicates the precipitation of a Ce conversion layer [50,63]; however, general identification of Ce in this particular sample was not possible by EDX, indicating that the precipitated layer must be very thin, confined to the nanoscale. The increased precipitation of Ce compounds on the sample post-treated in the CeP 50C solution may be associated with the facilitated formation of Ce(IV) complexes upon heating. Photographic documentation of the conversion solutions (not presented here, but available in [63]) showed that the CeP 50C post-treatment solution exhibited a yellow/orange colour, not presented by the others solutions, which remained either transparent or milky white. Moreover, previous XPS results [16] showed a predominance of Ce(IV) compounds on the surface of TSA-anodized clad AA2024-T3 alloy post-treated in a CeP 50C solution. In addition, the technical literature shows that Ce(IV) compounds are frequently yellow coloured, for instance, Cerium Ammonium Nitrate (CAN), which consists of a Ce(IV) coordinated with six $(NO_3)^-$ ions neutralized by a pair of NH_4^+ counter ions, is presented as an orange-red crystal [64]. Finally, Gordovskaya et al. [47] associated the intense yellow colour of some of their Ce conversion layers to increased presence of Ce(IV) compounds. However, albeit these evidences, further investigation is still necessary to unveil the role of temperature in the acceleration of Ce conversion layer precipitation.

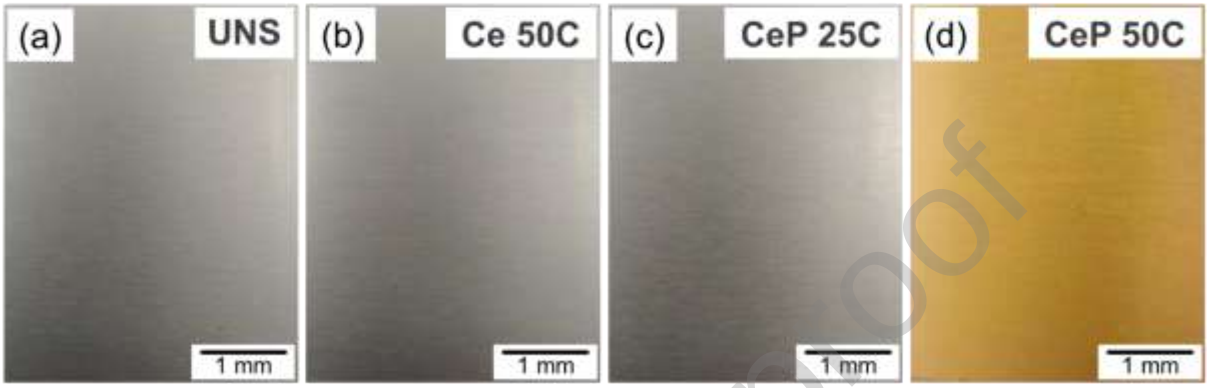

Figure 3. Digital images of the surfaces of the (a) UNS, (b) Ce 50C, (c) CeP 25C and (d) CeP 50C samples.

Figure 4 presents SEM magnified surface micrographs of UNS (a) and post-treated: Ce 50C (b), CeP 25C (c) and CeP 50C (d) samples. At this magnification, no significant alterations could be observed for the different samples, whose morphologies are similar to those reported in the literature for porous anodic layer [26,51]. However, the presence of sparsely distributed white precipitates was evident on the surface of the CeP 50C sample (Figure 4(d)), whose EDX analysis associated with its white colour showed to be oxygen-rich Ce compounds (Figure 5), frequently ascribed in the literature to the precipitation of mixed Ce oxy-hydroxides [16,45,47]. The images confirm that, whichever the post-treatment, no thick deposit was found in the oxide layer surface, thus keeping the top of the pores open, at variance with previously published works [29,47,50] and in consonance of the aim of the present investigation.

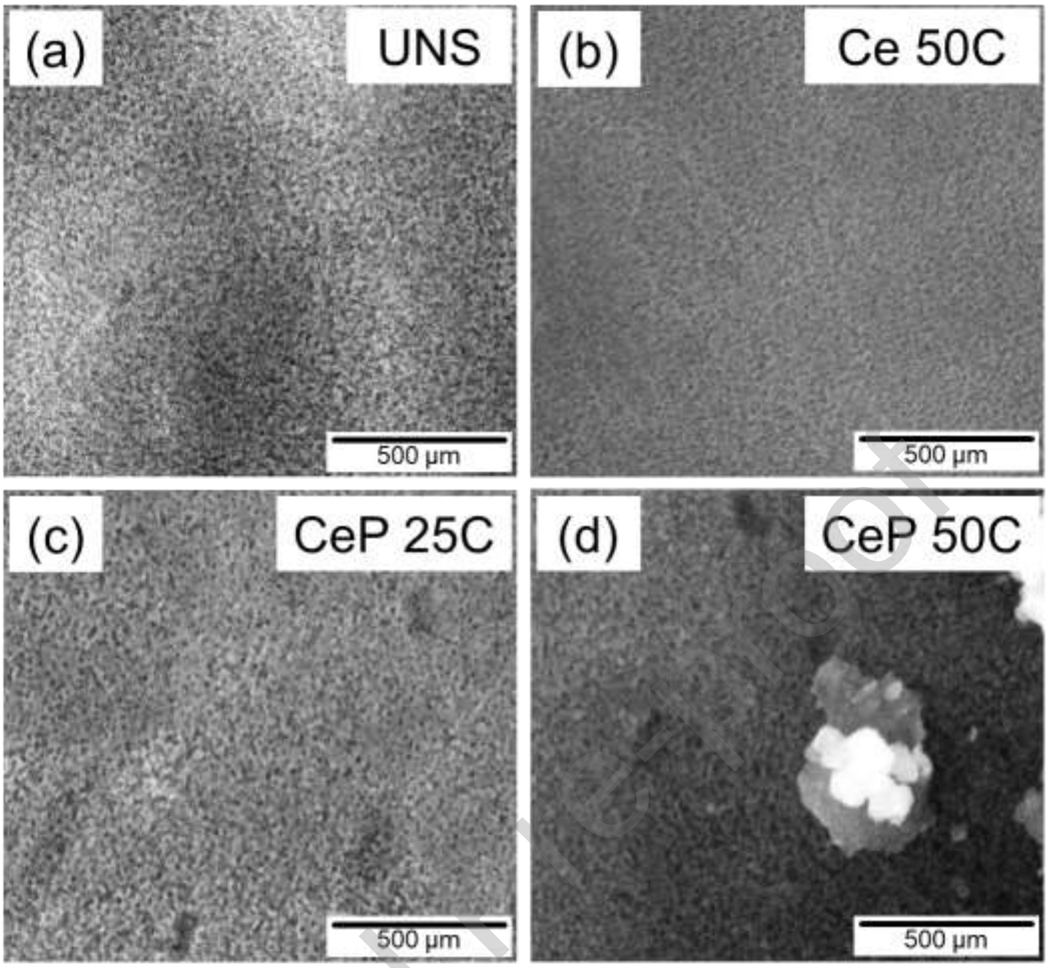

Figure 4. SEM micrographs of the AA2024-T3 anodized in TSA bath, (a) without (UNS) and after post-treatments: (b) Ce50C, (c) CeP 25C, (d) CeP 50C.

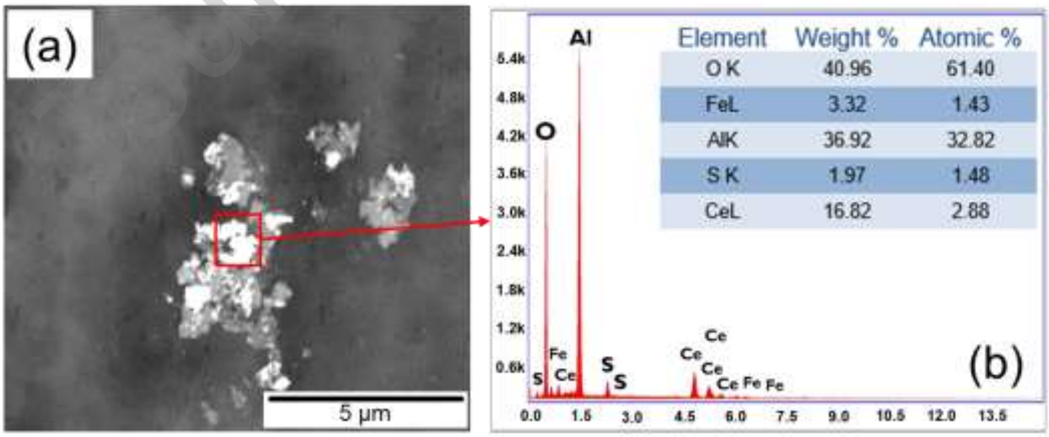

Figure 5. (a) SEM micrographs of the CeP 50C sample and (b) EDX analysis of the selected area.

Figure 6 shows a SEM image of a micrometric defective region on the surface of the anodic oxide layer of the CeP 50C sample associated with the EDX elemental compositional maps of the whole region. Besides Ce, the maps show the presence of Cu, Fe and Mn, indicating that it can be associated with a former large Cu-Fe-Mn IM. It is documented in the literature that, from Ce-rich aqueous solution, Ce oxy-hydroxides precipitates due to local increased surface pH associated with cathodic reactions [36–38,48]. From the two main IMs present in the microstructure of AA2024-T3: Al-Cu-Mg and Al-Cu-Fe-Mn, see Figure 1, the latter is always cathodic to the matrix [65,66]. The SEM-EDX analysis indicates that local cathodic activity associated with some of these sites still remains after the anodizing process, thus enhancing Ce deposition. The exploration of the surface of the samples submitted to the other pre-treatments did not allow to identify deposition of Ce at defective regions, indicating that they had insufficient oxidizing power to promote Ce deposition.

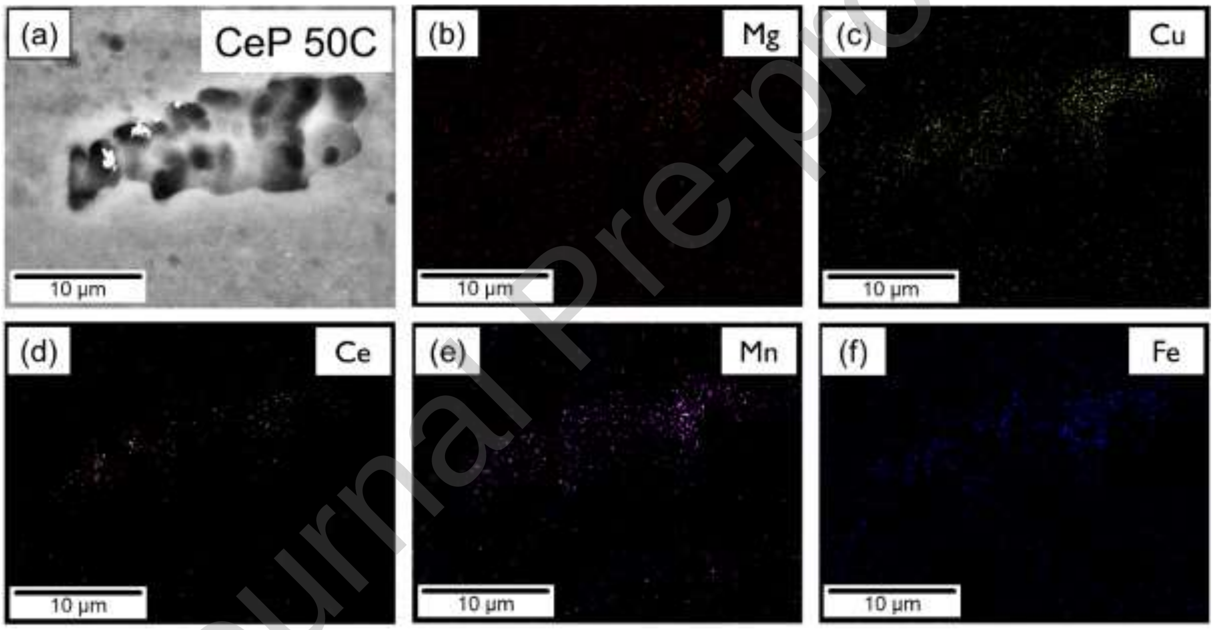

Figure 6. SEM-EDX characterization of a defective site at the surface of the anodic oxide layer of the CeP 50C sample.

3.2 Electrochemical characterization

3.2.1. Potentiodynamic polarization

Figure 7 presents the potentiodynamic polarization curves in 0.1M NaCl of the AA2024-T3 without (bare) and with the anodized layer: as produced (UNS) and with the different post-treatments. The anodic branch for the samples UNS, Ce 50C and CeP 25C show an increase of current from the corrosion potential (OCP). This is because the pitting potential of the alloy is around the OCP value. In the case of CeP 50C sample a quasi-passive region (about 200 mV) followed by a well-defined current increase is depicted, that could be associated with the pitting potential of the post-treated alloy with $Ce(NO_3)_3$ + H_2O_2 at 50 ºC.

However, in general the anodic behaviour shows an active response, indicating a relatively poor protection afforded by the different post-treatments, which can be ascribed to pitting starting at the flaws in the anodic film through which Al oxidation can takes place, as evidenced in Figure 2(c). This anodic active response is in accordance with Garcia-Rubio *et al.* findings for TSA and TSA-alodine post-treated samples in 0.5 M NaCl solution [26], ascribed to pitting onset just above the corrosion potential. However, this scenario changed when considering the cathodic response. In the case of the cathodic branch a more pronounced polarization could be observed for all anodized samples, with a reduction of about one order of magnitude of the current density in the diffusion-controlled region, pointing to oxygen as the main oxidant, which is also in accordance with Garcia-Rubio *et al.* [26] findings. This indicates that, overall, the anodizing process was successful in reducing cathodic sites on the electrode surface, and, therefore, the corrosion current density. Comparing only the anodized samples, polarization curves cannot clearly differentiate the corrosion behaviour of UNS, CeP 25C and Ce 50C samples, whereas a clear improvement was observed for the CeP 50C sample as a consequence of the increased polarization of the cathodic reaction. E_{corr} displayed in Table 2 shows lower values for the anodized samples, as a consequence of the polarization of the cathodic reaction, and, among them, CeP 50C sample showed the lowest E_{corr}.

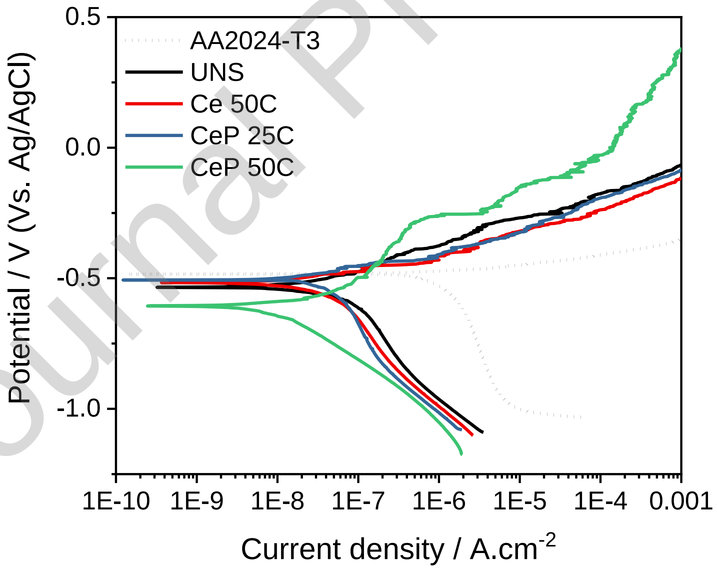

Figure 7. Polarization curves after 4h in NaCl 0.1M of AA2024-T3 anodized in TSA as-produced (UNS) and post-treated with the different protocols. As a reference the curve for a polished non-anodized AA2024-T3 sample is also presented.

Table 2. Corrosion potential for the different samples after 4h of immersion in NaCl 0.1M.

Samples	E_{corr} [V vs Ag/AgCl]
AA2024	-0.484 ± 0.005
UNS	-0.533 ± 0.003
Ce 50	-0.517 ± 0.006
CeP 25	-0.505 ± 0.007
CeP 50	-0.607 ± 0.002

3.2.2 EIS behaviour

Figure 8 depicts the EIS diagrams registered during 168 h (1 week) of immersion in the test electrolyte for the AA2024-T3 anodized in TSA as-produced (UNS) and with the different post treatments. After the completion of the tests the samples were damaged at different extents, as will be shown and discussed later. For each condition, as a reference, the diagram acquired after 4 hours immersion of a bare AA2024-T3 sample was added. Globally, the low frequency (LF) impedance modulus decreases as the immersion time elapses, indicating that the protection afforded by the layer is continuously deteriorating; however, this feature is sharper in the first 24 h of test. Independently of the sample condition, the phase angle diagrams evolve from a capacitive response spreading over a wide frequency range for short immersion times to a more complex behaviour that will be better discussed in the fitting with electrical equivalent circuit (EEC) procedure. Clearly, except for the CeP 50C sample, a LF time constant progressively develops for longer immersion times; however, the time necessary to the onset of this LF phenomenon is not the same for all the samples.

The evaluation of the time necessary for the different anodized samples to achieve a LF impedance modulus of the same order of magnitude of the non-anodized sample (AA2024-T3 4 h) can provide a preliminary insight about the long-term corrosion protection capability of the different systems. For the UNS sample (Figure 8(a)), this time span is only 24 h, for the Ce 50C (Figure 8(b)) and CeP 25C (Figure 8(c)): 96 h; whereas for the CeP 50C sample (Figure 8(d)), even after 168 h of test, the LF impedance modulus is about one order of magnitude higher than that exhibited by the non-anodized samples. Thus, this preliminary analysis demonstrates that, even though producing more corrosion resistant systems than the bare alloy for short immersion times (Figure 7 and EIS diagrams acquired after 4 h immersion in Figure 8), the capabilities of each system (without and with post-treatment) to retard the long-term corrosive process are different. Moreover, it also shows that, even though presenting similar polarization behaviour as the UNS sample after 4h immersion, samples CeP 25C and Ce 50C keep their corrosion protection ability for longer times.

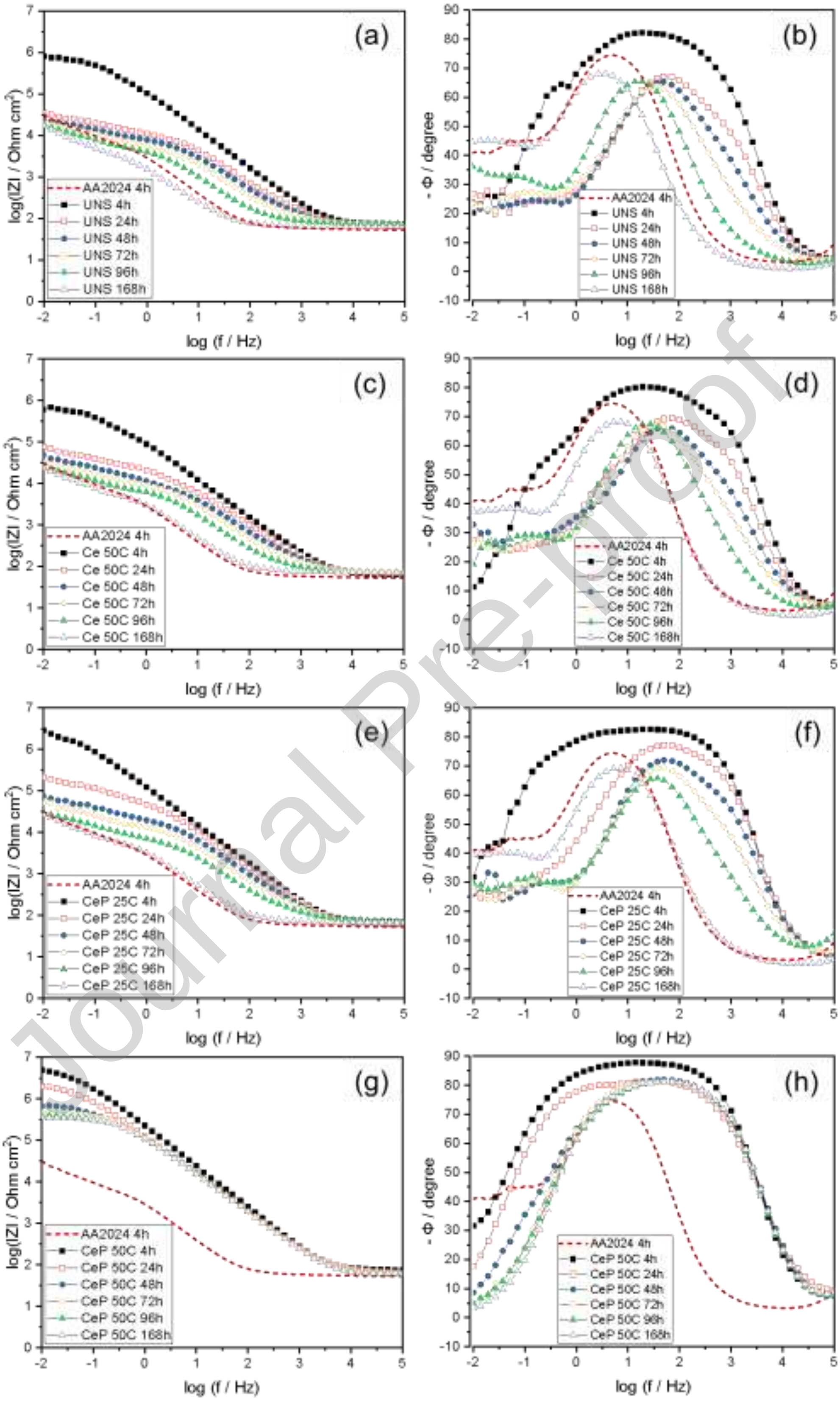

Figure 8. Bode plots of AA2024-T3 anodized in TSA: (a,b) as-produced (UNS) and post treated in (c,d) 50mM $Ce(NO_3)_3$ at 50°C (Ce 50C), (e,f) 50mM $Ce(NO_3)_3$ + H_2O_2 (10% v/v) at 25°C (CeP 25C), (g,h) 50mM $Ce(NO_3)_3$ + H_2O_2 (10% v/v) at 50°C (CeP 50C), obtained in

0.1 M NaCl solution until 168h. As a reference, the diagram for a polished non-anodized AA2024-T3 sample after 4 h of immersion is presented in each plot.

The impedance modulus at LF (10 mHz) for the whole set of samples after different immersion times is exhibited in Figure 9. This methodology is frequently employed to compare the anticorrosion performance of samples presenting similar EIS responses [16,34,46,52,67], to prove reproducibility, error bars were added for each condition. The figure shows that the CeP 50C sample presented the highest impedance modulus during the whole test period, as well as a more stable response, characterized by a slower decrease of the impedance modulus. For this sample, at the first immersion hours, the LF impedance modulus is of the same order of magnitude of similar substrate with different sealing processes [26,29,50,51,68] and also submitted to Alodine® post-treatment [26]. However, it was not possible to compare the time evolution of the CeP 50C impedance modulus with previous published data due to the lack of long-term electrochemical tests for protection systems using the same substrate (AA2024-T3) and with a similar structure (anodic layer topped with a Ce conversion coating) [47,50].

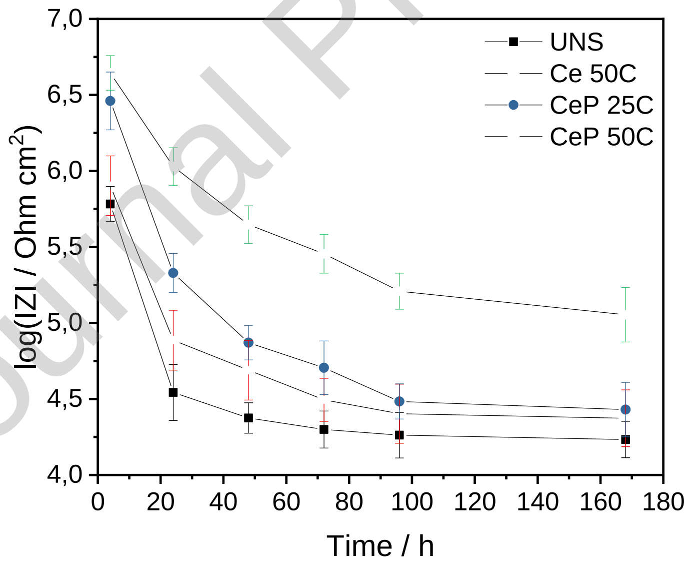

Figure 9. Evolution with immersion time in NaCl 0.1 M of the impedance modulus at 10 mHz for AA2024-T3 anodized in TSA: as-produced (UNS) and post treated with the different experimental protocols.

Figure 10 depicts the EECs used to fit the EIS diagrams for the different samples; they were conceived considering the variation of the EIS responses with immersion time as a consequence of degradation due to corrosion. Frequently, it was necessary to replace the capacitors for constant phase elements (CPE) to consider the non-ideal behaviour of the interface [11,16,29,69,70].

The EEC of Figure 10(a) is similar to others employed in the literature for slightly damaged anodic layers [11,16,52,54,69,71–73], and considers that, at short immersion times, the pore structure is open and the corrosion process takes place at the flaws of the barrier layer; CPEb and Rb correspond, respectively, to the capacitance and resistance of the pores (defects) of the barrier layer, whilst Rct and CPEdl account for the charge transfer resistance and the double layer capacitance. At this stage, the electrolyte can easily reach the interface through the open pore structure, and corrosion is mild at the barrier layer flaws, resulting in relatively high impedance modulus.

The EEC of Figure 10(b) was employed to fit a major part of the EIS diagrams of the post-treated samples, except CeP 50C. The physical model points to precipitation of corrosion products inside the pores (Rp//Cp), acting as a protective barrier (partial sealing) [12,15,16,52], and that the EIS measurements no longer detect the resistance of the barrier layer, indicating increased corrosion activity at the defective regions due to enlargement of defective sites (Rb <<< Rct). Moreover, a finite diffusion-controlled process was detected in the LF region, which is characterized by a flat phase angle in the Bode diagrams (see Figure 8) and by a straight line in the Nyquist diagrams (not presented). At this stage, impedance moduli steadily decrease, indicating that, even though retarding the deterioration of the samples, the blocking corrosion products are not able to impede aggressive species to reach the interface, and corrosion activity is enhanced with immersion time.

The evolution of the EIS response described in the two previous paragraphs is supported by recent findings by Ma *et al.* [59] on the corrosion behaviour of AA2025 anodized in TSA, which were drawn by means of careful SEM observation of the cross-section of corroded areas. According to these authors [59], the localized corrosion of the anodized Al alloy can be divided in two stages: in the early immersion period, when corrosive activity is low, corrosion is controlled by the inward diffusion of aggressive electrolyte and the outward diffusion of corrosion products through the anodic film and the material does not present noticeable corrosion, indicating a slow process; in the later stage, rapid propagation of localized corrosion takes place due to direct access of the aggressive electrolyte to the underneath Al matrix at defective sites of the anodic film, most frequently associated to cavities generated by incomplete oxidation of IMs, sites at which a defective barrier layer is generated (see Figure 2(c)). The EEC represented in Figure 10(a) is associated with the early stage of corrosion, whereas the EEC of Figure 10(b) characterizes the later stage of the process described by Ma *et al.* [59]. Diffusion of species through the corrosion products precipitated within the pores would account for the LF diffusion-controlled process.

The EIS responses of the UNS (for immersion times longer than 96 h) and CeP 50C (from 24 h on) samples, represented, respectively, by EEC of Figure 10(c) and 10(d), largely differ from those previously reported. For the former sample, after 96 h of test, the corrosion products precipitated inside the pores are no longer detected by the EIS measurements for either or both of the two reasons: the corrosion products (formed by aluminium oxy-hydroxides) are less stable and/or the anodic layer is greatly damaged (see Figure 12(b)). On the other hand, for the CeP 50C sample, the corrosion products precipitated inside the pores, even though with decreasing protection tendency (impedance modulus decreases with time), continue to be an effective barrier against corrosion, thus retarding the kinetics of the interfacial processes (note that EEC (d) corresponds to EEC (b) without the LF diffusion-controlled process).

Electrical equivalent circuits	UNS	Ce 50C	CeP 25C	CeP 50C
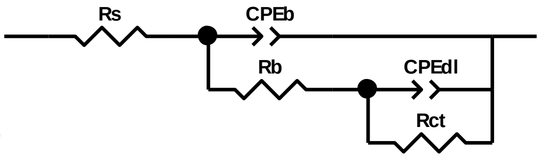 (a)	**4h**	**4h**	**4h**	**4h**
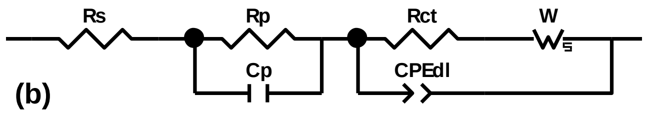 (b)	**24-72h**	**24-168h**	**24-168h**	**-**
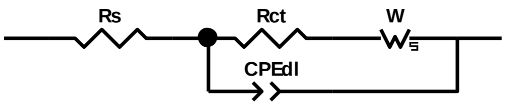 (c)	**96-168h**	**-**	**-**	**-**
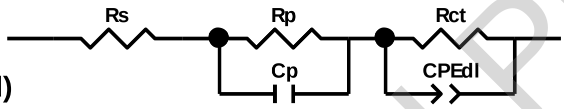 (d)	**-**	**-**	**-**	**24-168h**

Figure 10. Electrical equivalent circuits (EEC) used to fit the EIS diagrams of all the samples, with the periods for which each of the circuit was used for the different samples.

Table 3 presents the results of the fitting procedure. After 4 h, both Rb and Rct are relatively high, confirming the low corrosion activity; the sparse corrosion products formed during this period precipitate within the pores, close to defective sites, but they are not sufficient to provoke their partial blockage. Rb is about one order of magnitude higher for the samples post-treated in the solutions containing H_2O_2 (CeP 25C and CeP 50C), indicating a positive impact of H_2O_2 addition to the post-treatment bath in the protective properties of the oxide layer, which seems to become less defective. From 24 hours on, globally, there is a tendency to a Rp decrease and a Cp increase with immersion time. This can be ascribed to the continuous ingress of aggressive species, reducing the protective nature of the corrosion products, which, nevertheless, are present at increased amounts, associated with the damage of the porous layer. In accordance with its superior performance, Rp is much higher and Cp smaller and more stable for the CeP 50C sample, indicating a more protective nature of the corrosion products (Ce oxy-hydroxides, as indicated in Figure 12). In accordance with the increased deterioration of the corrosion resistance of the oxide layer, for the whole set of samples, Rct decreases, indicating easier electrochemical reactions at the interface, and Cdl increases, as a consequence of a larger exposed unprotected area. Finally, the resistance associated with the diffusion process (R-W) exhibits unexpected high values for the UNS sample. This can be related to the large amount of corrosion products precipitated on the surface of this particular sample; however, the small Rct values determined in the EEC fitting procedure indicates that corrosion products are non-protective, which was confirmed by the visual analysis of the sample (Figure 11). The sum of the resistive elements of the fitting procedure throughout the test period corresponds to the same corrosion resistance ranking previously identified: CeP 50C > CeP 25C > Ce 50C > UNS.

Table 3. Results of the fitting procedure of the EIS diagrams with the EECs of Figure 10 for the AA2024-T3 anodized in TSA without and with the different post-treatments. “n” stands for the exponent of the CPE.

				UNS							
Time (h)	Rs (Ω.cm^2)	Rp (Ω.cm^2)	Cp (F.cm^{-2})	Rb (Ω.cm^2)	CPEb (F.cm^{-2}.S$^{(n-1)}$)	nb	Rct (Ω.cm^2)	CPEdl (F.cm^{-2}.s$^{(n-1)}$)	ndl	R-W (Ω.cm^2)	nw
4	68			3.32E+5	1.74E-6	0.92	4.49E+5	2.17E-6	0.81		
24	61	3552	6.84E-6				1.05E+4	1.92E-5	0.72	2.22E+5	0.42
48	66	3268	9.27E-6				5.46E+3	3.71E-5	0.68	8.64E+4	0.34
72	72	2379	1.33E-5				9.79E+3	7.43E-5	0.65	1.82E+5	0.50
96	78						4.30E+3	2.58E-5	0.87	2.61E+5	0.54
168	57						3.39E+3	1.14E-4	0.90	2.49E+4	0.53
				Ce 50C							
Time (h)	Rs (Ω.cm^2)	Rp (Ω.cm^2)	Cp (F.cm^{-2})	Rb (Ω.cm^2)	CPEb (F.cm^{-2}.S$^{(n-1)}$)	nb	Rct (Ω.cm^2)	CPEdl (F.cm^{-2}.s$^{(n-1)}$)	ndl	R-W (Ω.cm^2)	nw
4	71			3.81E+5	1.75E-6	0.90	4.14E+5	3.03E-6	1.00		
24	66	1479	9.60E-6				2.78E+4	6.67E-6	0.80	1.21E+5	0.50
48	69	2886	7.54E-6				2.12E+4	2.28E-5	0.70	1.34E+5	0.50
72	69	4716	8.15E-6				2.09E+4	5.97E-5	0.63	7.72E+4	0.50
96	70	4036	1.36E-5				2.53E+4	1.22E-4	0.63	1.69E+4	0.50
168	73	2508	7.36E-5				6.57E+3	1.64E-4	0.77	1.58E+4	0.50
				CeP 25C							
Time (h)	Rs (Ω.cm^2)	Rp (Ω.cm^2)	Cp (F.cm^{-2})	Rb (Ω.cm^2)	CPEb (F.cm^{-2}.S$^{(n-1)}$)	nb	Rct (Ω.cm^2)	CPEdl (F.cm^{-2}.s$^{(n-1)}$)	ndl	R-W (Ω.cm^2)	nw
4	70			1.38E+6	1.42E-6	0.93	1.33E+6	8.46E-7	1.00		
24	60	11919	3.85E-6				8.16E+4	4.43E-6	0.84	3.28E+5	0.50
48	57	7985	4.08E-6				2.73E+4	1.48E-5	0.74	1.29E+5	0.50
72	62	6243	6.24E-6				1.31E+4	2.60E-5	0.69	2.91E+4	0.52
96	69	3666	1.00E-5				2.75E+4	8.22E-5	0.61	3.71E+4	0.50
168	68	2970	6.54E-5				1.69E+4	1.82E-4	0.75	1.36E+4	0.55
				CeP 50C							
Time (h)	Rs (Ω.cm^2)	Rp (Ω.cm^2)	Cp (F.cm^{-2})	Rb (Ω.cm^2)	CPEb (F.cm^{-2}.S$^{(n-1)}$)	nb	Rct (Ω.cm^2)	CPEdl (F.cm^{-2}.s$^{(n-1)}$)	ndl	R-W (Ω.cm^2)	nw
4	73			4.08E+06	7.88E-07	0.97	3.20E+06	5.56E-06	1.00		
24	64	380310	3.92E-06				1.79E+06	2.50E-06	0.87		
48	58	97732	2.41E-06				5.88E+05	3.18E-06	0.86		

72	60	56659	3.90E-06		3.97E+05	2.28E-06	0.89
96	60	40222	3.45E-06		3.42E+05	2.43E-06	0.89
168	58	18941	6.30E-06		3.20E+05	1.93E-06	0.90

3.3 Analyses of corroded samples

Figure 11 displays optical micrographs of the different samples before (a, c, e, g) and after (b, d, f, h) the completion of the EIS tests. All of them presented pitting corrosion; however, the intensity of the surface attack is well in agreement with the results of the impedance tests. Except for the CeP 50C, at which pits were smaller and uniformly distributed, large pits could be identified in the other samples (encircled black spots). They are generally surrounded by a corrosion product ring, inside of which a zone relatively free from corrosion can be identified, well in agreement with the severe localized corrosion (SLC) sites pointed out by Ma *et al.* [74] for Al-Li alloys. The images also attest a stronger overall surface damage for the UNS sample and show that the CeP 50C sample is better preserved.

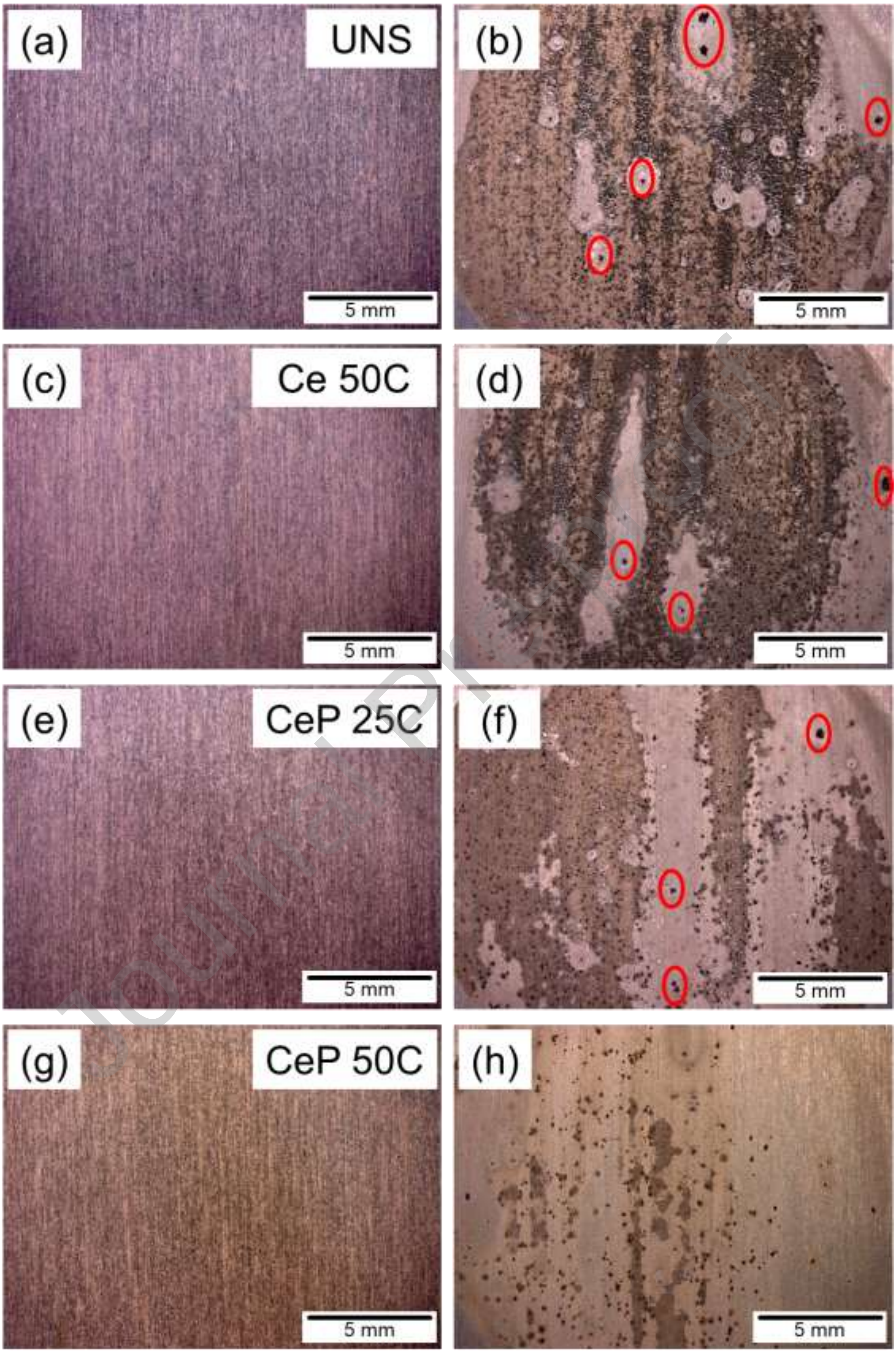

Figure 11. Optical micrographs of the surface of the (a,b) UNS, (c,d) Ce 50C, (e,f) CeP 25C, and (g,h) CeP 50C samples, before (a,c,e,g) and after (b,d,f,h) 168 h of immersion in 0.1 M NaCl. Large pits are highlighted in the different images by means of red circles.

Figure 12 shows SEM images of the whole set of samples after 168 h (1 week) immersion in 0.1 M NaCl solution. The cracked patterns presented in the lower magnification micrographs (Figure 12 (a), (d), (g), (j)) are similar to those presented by Ma *et al.* [59], and can be associated to the localized corrosion process occurring in the matrix underneath the anodic layer, after corrosion initiation at defective sites. The EDX analysis (Figures 12 (c), (f), (i), (l)) of the brighter spots presented in the higher magnification micrographs (Figures 12 (b), (e), (h), (k)) showed large amounts of Cu, indicating that, independently of the sample, stable localized corrosion sites are established near Cu-rich IM of the parent alloy, underneath the oxide layer, similarly to the mechanism of localized corrosion proposed for bare AA2024-T3 alloy, stating that pitting corrosion propagates in relatively large clusters of IMs buried beneath the alloy surface [8,66,75]. Ce oxides were identified in the corrosion product of the less damaged CeP 50C sample, indicating that their precipitation may act to retard the corrosion process.

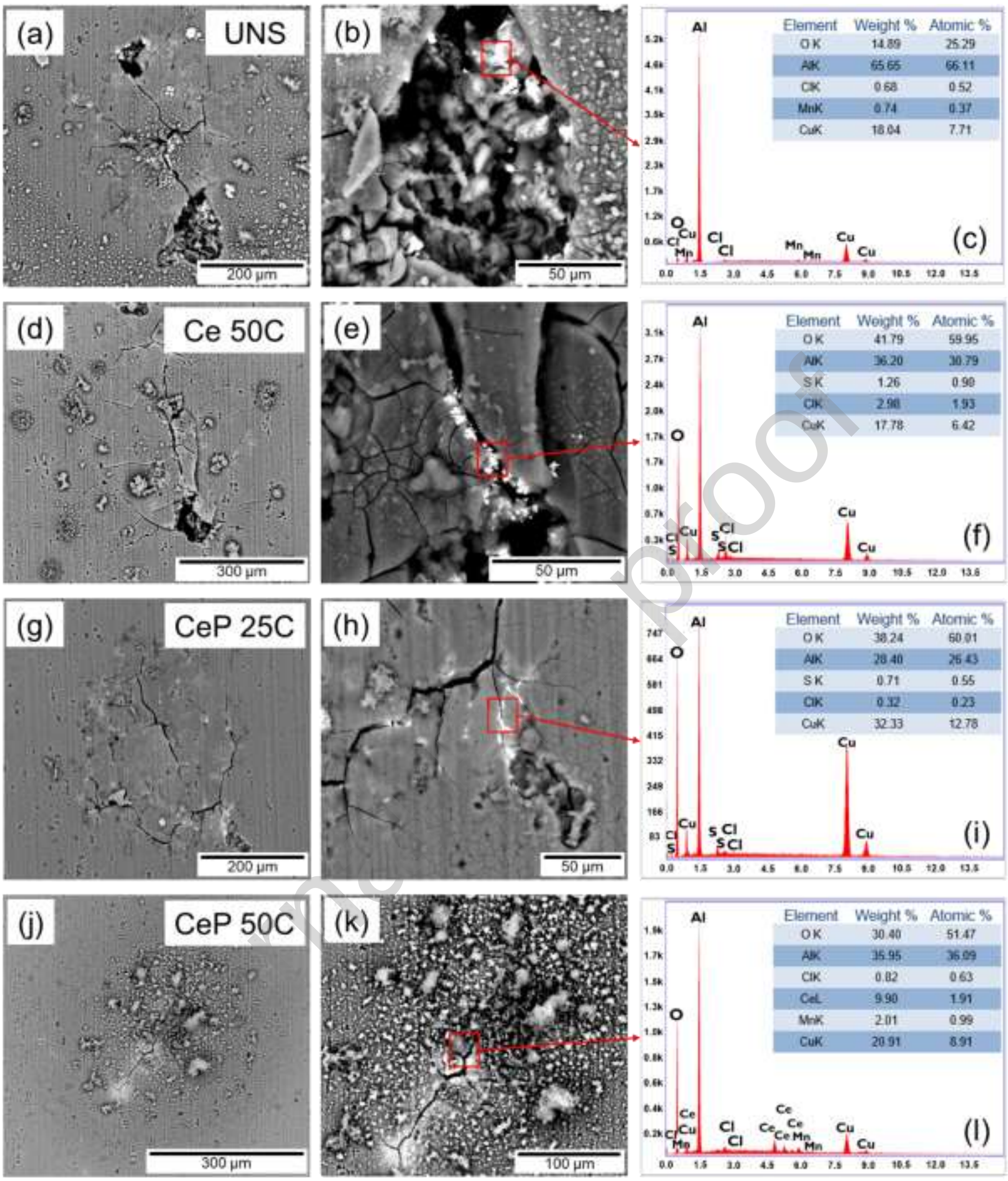

Figure 12. SEM micrographs and EDX analyses of defects on the surface of (a,b,c) UNS, (d,e,f) Ce 50C, (g,h,i) CeP 25C, (j,k,l) CeP 50C samples after 168 h immersion in NaCl 0.1M.

4. Characterization of the anodic layer of the CeP 50C sample

For the specimen presenting the best corrosion behaviour, CeP 50C, a detailed investigation was performed in order to evaluate Ce distribution in the anodic layer. In some instances, results for the UNS sample are presented as a reference.

4.1 AFM analysis

Figure 13 shows AFM micrographs of UNS and CeP 50C samples where a smoother coverage is associated with this latter sample. The root mean-square roughness parameter (RMS) was determined to be 66.9 nm for UNS sample and 58.5 nm for the CeP 50C, indicating a slight decrease in surface roughness with the post-treatment. Often, anodizing affects the surface finish of the aluminium substrate, due to dissolution of microstructural components in the anodizing bath [76], being the extent of change in the surface roughness largely dependent on the type of the anodic process performed. The smoother surface revealed for the CeP 50C sample can be a consequence of the precipitation of the Ce conversion layer on top of the porous layer (see Figure 3), and the coverage of defective sites associated with IMs in the micrometre range (usually cathodic due to Cu and Fe enrichment), see Figure 6.

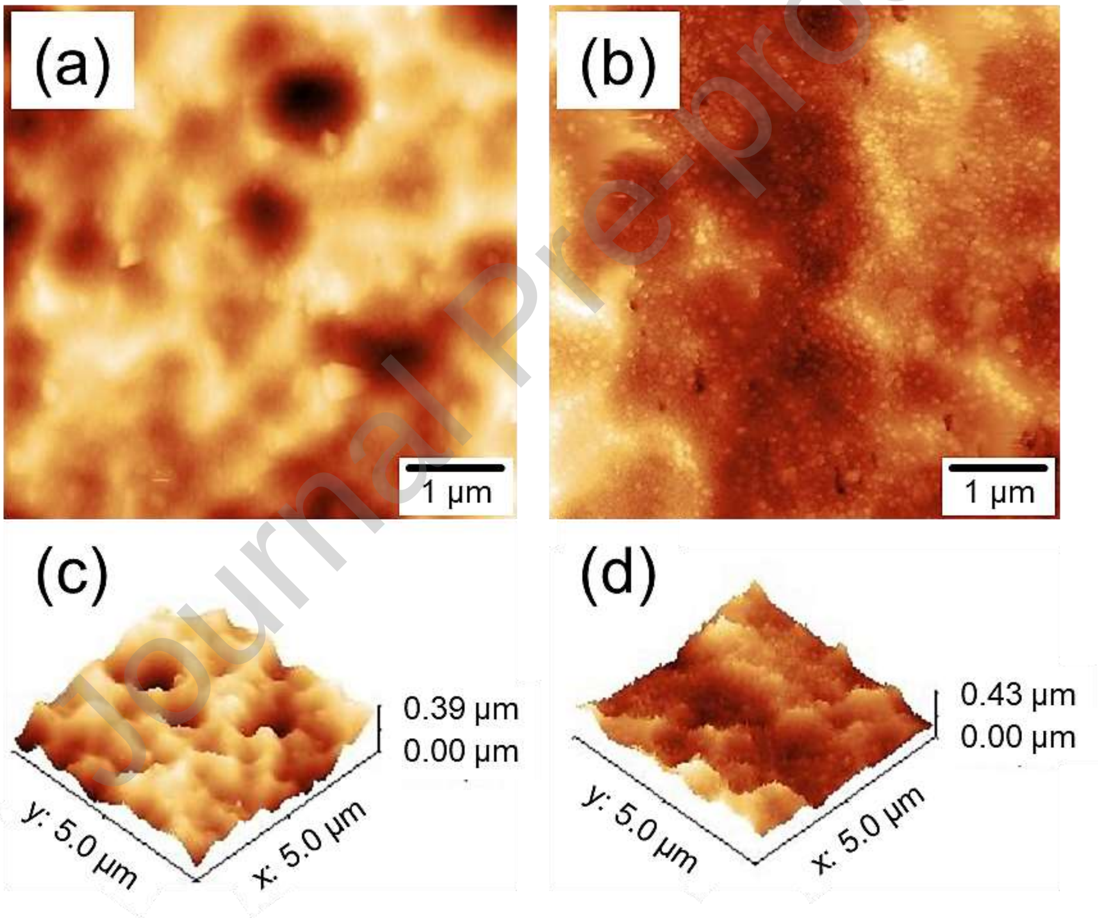

Sample	RMS (nm)
UNS	66.9
CeP 50C	58.5

Figure 13. AFM topography images of anodized samples without post-treatment – UNS: (a) and (c); and post-treated with 50 mM $Ce(NO_3)_3.6H_2O$ + H_2O_2 (10% v/v) at 50°C - CeP 50C (b) and (d). Table: root mean square roughness parameter (RMS) determined by AFM of the analysed samples.

4.2 GDOES analysis

Depth profiles of the UNS and CeP-50C sample were assessed by means of GDOES and are presented in Figure 14. Besides the elements already reported in other works with TSA-anodized samples: Al, O and S [11,16,26,34], the depth profiles also show the presence of small amounts of Ce (CeP-50C) through the whole oxide layer thickness with an increased amount accumulated at the pores bottom, as indicated by the bump in the quantitative depth profile (Figure 14(b)), which is in accordance with previously reported results [16]. Considering the O profile as a reference, a thickness of about 3.0 – 3.5 µm can be estimated for the oxide layer of the two samples. The broad Al interface can be a consequence of the roughness of the AA2024-T3 used in the as-received condition after some chemical etching procedures, as described in the experimental part.

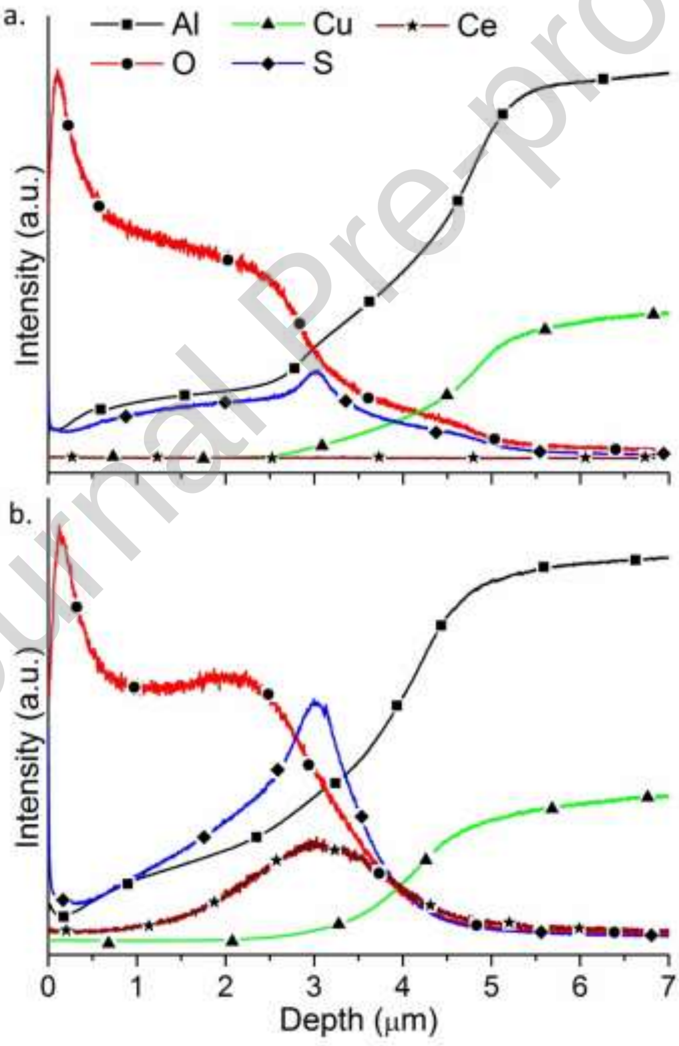

Figure 14. GDOES depth profiles of (a) UNS sample and (b) CeP 50C sample.

4.3 Scanning transmission electron microscopy (STEM) characterization

The cross-section of the anodic layer onto the CeP 50C sample is shown in bright-field TEM (BFTEM) micrograph in Figure 15. In good agreement with the SEM and GDOES analysis, the anodic layer was found to have a thickness around 3.5 μm in average (micrograph not presented). The cross-section reproduces features already revealed by other authors for TSA anodic layers produced in AA2024-T3 [12,73,77] and is clearly divided in two different regions: near the substrate surface (top image), at which fresh oxide is produced, a *quasi*-tubular structure reproduces fairly well the regular pores pattern expected for an Al anodic layer [11,16,78–80], on the other hand, lateral porosity, which can be evidenced using Fresnel contrast either under or in overfocus condition, characterizes the top region of the layer (bottom images). This latter region was regular and spreads over the upper part of the cross-section (about two third of the total thickness) and its morphology was noted to be composed of a dual character: some porosity resembling spherical voids, but an intricated network of lateral tubular-shaped voids constitutes a major part of the porous morphology (see details in Figure 16(a)). Another interesting observation made with BFTEM is the presence of regions where voids are more pronounced, as exhibited in the white circle in Figure 15 (top micrograph): in this region (herein referred as a “defective region”), both size and density of the pores are higher than in the overall layer. The diffraction pattern displayed in Figure 16(b) confirmed the amorphous nature of the anodic layer. Lateral porosity has been reported for anodic layers formed on AA2024-T3 substrates [12,73,79]. Torrescano-Alvarez et al. [79] ascribed this feature to oxygen generation triggered by the incorporation of copper oxide nanoparticles in the anodized layer, whereas the defective region can be generated at sites of incompletely oxidized former IM particles; experimental evidences of both processes will be presented in the next paragraphs.

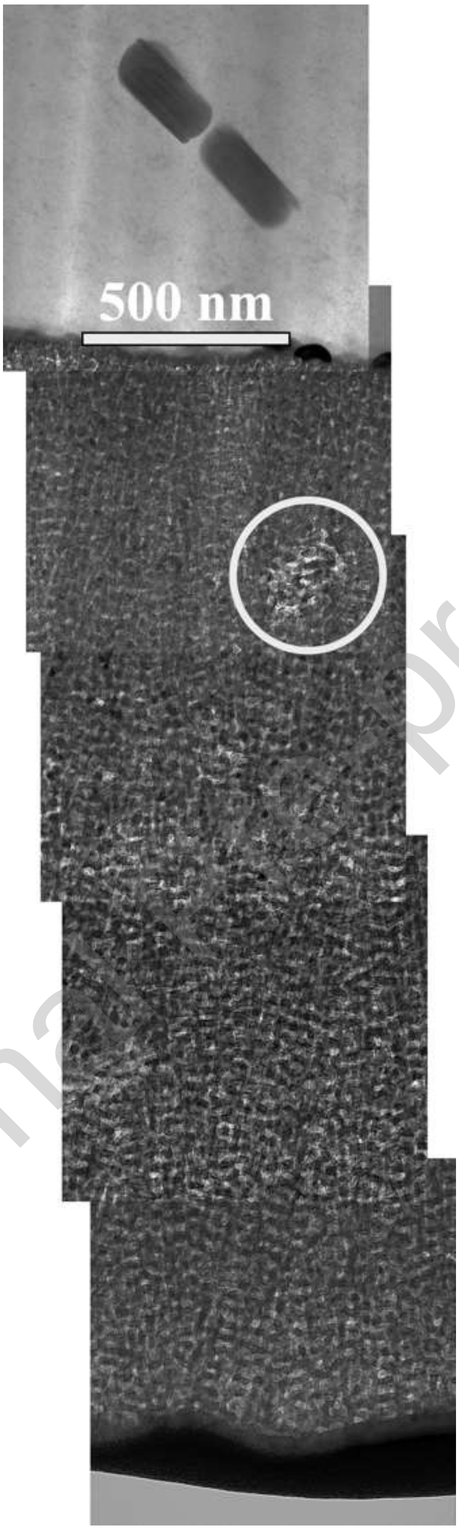

Figure 15. BFTEM cross-section of the anodic layer of the CeP 50C sample. The anodic layer has a thickness of around 3.5 μm. The images were acquired in underfocus condition and show the porous regions in brighter contrast. The defocus degree for the image is –2 μm. Top image corresponds to the substrate-oxide layer interface, whereas the bottom image corresponds to the top of the anodized layer.

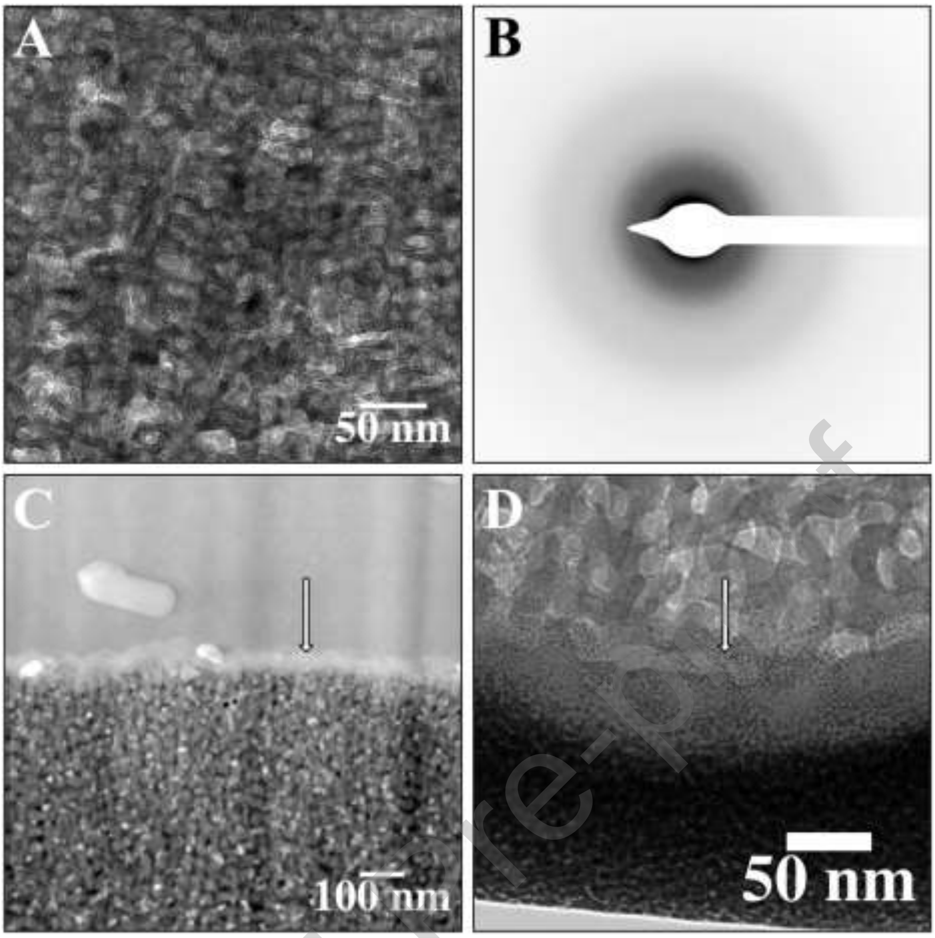

Figure 16. Porous structure and diffraction pattern of the anodized layer on CeP 50C sample are shown in (a) and (b), respectively. The HAADF micrograph in (c) shows in detail the presence of the barrier layer in between the AA2024-T3 substrate and the porous layer: thickness of around 30-40 nm. BFTEM micrograph in (d) shows the presence of a layer between the Pt protective coating (black contrast) and the anodic layer with a thickness of around 50 nm. Note: micrographs (a) and (d) were taken with –800 nm and –2.0 μm defocus, respectively.

Two regions of interest are noted in Figure 16: the presence of a strong dark contrast between the AA2024-T3 substrate and the porous layer (Figure 16(c)) and a continuous and homogenous layer on the top of the lamella (Figure 16(d)), both of them indicated by white arrows. The first – the barrier layer – is depicted in detail in the high-angle annular dark-field (HAADF) micrograph in Figure 16(c), presenting a thickness of around 30-40 nm. The layer on top of the lamella – an oxide – is shown in the BFTEM micrograph in Figure 16(d), presenting a thickness of around 50 nm. EDX analysis of this latter layer showed a high amount of Pt, indicating an interaction between the Pt deposit and the oxide layer.

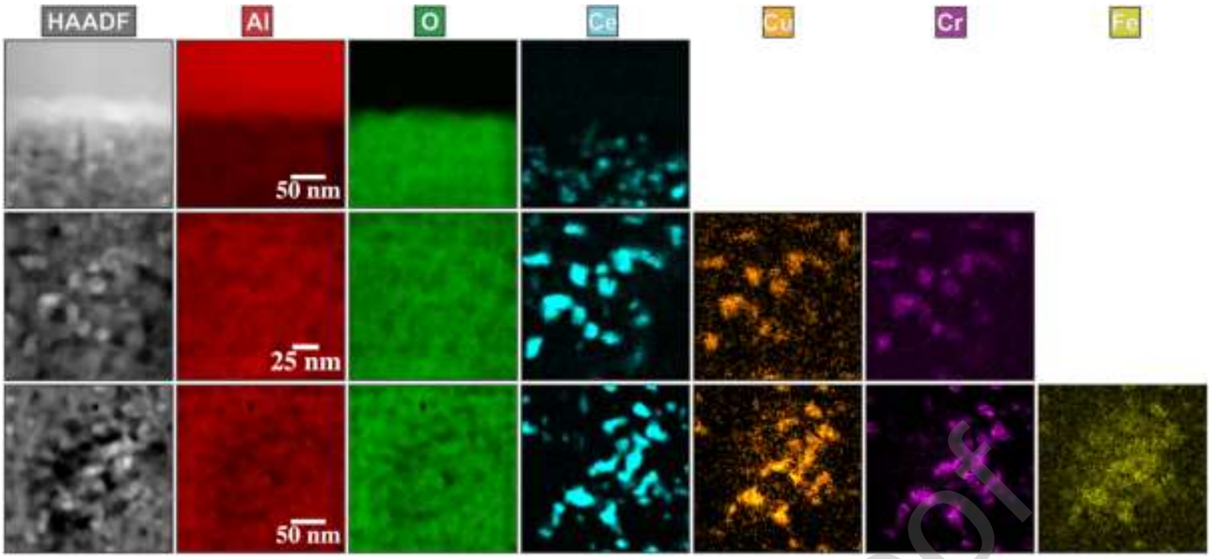

Figure 17. STEM-EDX mapping of three distinct regions of the anodic layer on CeP 50C sample: top row shows the interface between the AA2024-T3 substrate and the anodic layer, middle row was collected in the middle of the anodic layer and the bottom row shows mapping around a defective region within the anodic layer (as indicated in the white circle in Figure 15). Note: The element S has been identified in all regions and its maps are not shown for clarification.

To investigate the composition of the anodic layer and to evaluate the Ce distribution along its cross-section, STEM mapping with EDX spectroscopy was used. Figure 17 top image depicts STEM-EDX maps of Al, O and Ce over the interface with the AA2024-T3 substrate, in the middle of the lamella and around the defective region shown in the white circle in Figure 15 (bottom image), for the two latter regions maps of relevant elements were added. Concerning the porous layer composition, the EDX maps revealed the presence of Cu-rich regions within the bulk anodic layer (maps acquired at the central region), supporting the hypothesis that oxygen evolution at semiconducting Cu oxide may generate the lateral porosity observed in the anodic layer [12,73,79], in addition, Cu and Fe enrichment at the "defective region" (bottom image) indicates the incorporation of remnants of non-completely oxidized IMs within the anodic layer microstructure. Interestingly, Cr-enrichment was also detected at the two Cu-enriched regions; to the best of the authors knowledge, this feature has never been previously reported, and indicates that Cr added to achieve grain refinement [53] may redeposit during anodizing at regions at which oxygen evolution is favoured, the mechanism behind this process remains to be investigated.

The maps of Figure 17 show that Ce-rich nanoparticles deposition starts immediately after the barrier layer (see the top image) and are quite uniformly distributed throughout the anodic layer cross-section, proving Ce deposition within the pores. Nevertheless, heavier Ce deposition was observed near Cu (and Cr) enriched regions. This was an important outcome in the frame of the corrosion protection mechanism afforded by Ce conversion coatings previously discussed [47,49–51] as it shows that Ce nanoparticles also covers cathodic sites within the inner structure of the porous layer, indicating hinderance of degradation due to corrosion also at the nanoscale level in the porous structure of the anodized layer.

The STEM-images of Figure 17 were also used to estimate the mean diameter of the Ce nanoparticles and the outcome was the following: 12.9 ± 1.7 nm at the interface (pores bottom), 9.5 ± 1.6 nm in the middle of the layer and 12.2 ± 1.8 nm in the defective region. These results are well in agreement with the GDOES findings, indicating an accumulation of Ce at the pores bottom; however, the average diameter of the nanoparticles was smaller than that determined for a clad AA2024-T3 sample submitted to this same surface treatment procedure: 16.39±0.04 nm [16], even though the areal density (not determined) of Ce nanoparticles was visibly higher for the sample investigated in the present work. The smaller size of the Ce nanoparticles allied with their higher areal density is well in agreement with crystal nucleation principles at which, for a given solution concentration and nucleation condition, the higher the number of stable nuclei the smaller the crystals sizes [81,82].

5. Conclusions

In this work, the corrosion resistance of AA2024-T3 anodized in TSA and post-treated for 2 minutes in solutions containing 50 mM of cerium nitrate, without or with 10% (w/w) H_2O_2, was studied, two temperatures were investigated in the H_2O_2 containing solution: 25 ^oC and 50 ^oC. The polarization curves and the EIS experiments disclosed that the post-treatment consisting in the immersion of the samples in the H_2O_2 containing bath at 50°C was the most efficient to improve the corrosion resistance while maintaining the open structure of the pores of the anodic layer, as confirmed by SEM analysis. SEM-EDX surface analysis of the samples post-treated in this solution, before and after the corrosion tests, showed the presence of Ce precipitates in the vicinity of Cu-rich cathodic regions. For the corroded samples, Ce precipitates were frequently found in the vicinity of defective regions of the anodic oxide layer, indicating that these ions can be released and act as corrosion inhibitors.

Detailed analysis of the CeP 50C sample by AFM showed a smoother surface after the Ce post-treatment suggesting the precipitation of a Ce conversion layer on top of the anodized porous layer, confirmed by the yellow colour exhibited by the macroscopic sample, and the partial coverage of surface defective sites associated with IMs. Furthermore, GDOES analysis revealed the presence of Ce through the whole thickness of the oxide layer, indicating the precipitation of Ce-rich particles within the pores, with higher concentration at the pores bottom.

BFTEM of CeP 50C confirmed the development of lateral porosity in the porous layer structure, which, according to the literature, is developed due to Oxygen evolution in semiconducting Cu particles, the presence of this latter element within the whole thickness of the anodic oxide layer was confirmed via STEM-EDX mapping. STEM-EDX maps also showed that Ce oxide nanoparticles are distributed through the length of the pores of the anodic layer. However, an accumulation of Ce nanoparticles was indicated both at the bottom of the pores and at defective regions of the anodic oxide layer characterized by Cu enrichment, showing that Ce may contribute to hinder the corrosion process also at the nanoscale.

Acknowledgements

HG de Melo is thankful to FAPESP Proc. 2018/01096-5 and CNPq Proc. 400895/2014-5 for the financial support to the project

O.M. Prada Ramirez is thankful to CAPES Proc. 88887.388129/2019-00

This study was financed in part by the Coordenação de Aperfeiçoamento de Pessoal de Nível Superior - Brasil (CAPES) - Finance Code 001

MAT acknowledges present research support from the Laboratory Directed Research and Development Program of the Los Alamos National Laboratory under project number 20200689PRD2.

C. Neves and M. G. S. Ferreira acknowledge research support from CICECO - Aveiro Institute of Materials, trough project UIDB/50011/2020 & UIDP/50011/2020, financed by national funds through the Portuguese Foundation for Science and Technology/MCTES.

Data Availability

The raw/processed data required to reproduce these findings cannot be shared at this time as the data also forms part of an ongoing study.

References

[1] ASM International, The Effects and Economic Impact of Corrosion, in: Corros. Underst. Basics, 2000: pp. 1–21.

[2] M.A. Tunes, L. Stemper, G. Greaves, P.J. Uggowitzer, S. Pogatscher, Prototypic Lightweight Alloy Design for Stellar-Radiation Environments, Adv. Sci. 7 (2020) 1–11. https://doi.org/10.1002/advs.202002397.

[3] A. Boag, A.E. Hughes, N.C. Wilson, A. Torpy, C.M. MacRae, A.M. Glenn, T.H. Muster, How complex is the microstructure of AA2024-T3?, Corros. Sci. 51 (2009) 1565–1568. https://doi.org/10.1016/j.corsci.2009.05.001.

[4] A.E. Hughes, A.M. Glenn, N. Wilson, A. Moffatt, A.J. Morton, R.G. Buchheit, A consistent description of intermetallic particle composition: An analysis of ten batches of AA2024-T3, Surf. Interface Anal. 45 (2013) 1558–1563. https://doi.org/10.1002/sia.5207.

[5] N. Birbilis, R.G. Buchheit, Electrochemical Characteristics of Intermetallic Phases in Aluminum Alloys An Experimental Survey and Discussion, J. Electrochem. Soc. 152 (2005) B140–B151. https://doi.org/10.1149/1.1869984.

[6] K.S. Ghosh, M. Hilal, S. Bose, Corrosion behavior of 2024 Al-Cu-Mg alloy of various tempers, Trans. Nonferrous Met. Soc. China (English Ed. 23 (2013) 3215–3227. https://doi.org/10.1016/S1003-6326(13)62856-3.

[7] W. Zhang, G.S. Frankel, Transitions between pitting and intergranular corrosion in AA2024, Electrochim. Acta. 48 (2003) 1193–1210. https://doi.org/10.1016/S0013-4686(02)00828-9.

[8] X. Zhou, C. Luo, T. Hashimoto, A.E. Hughes, G.E. Thompson, Study of localized corrosion in AA2024 aluminium alloy using electron tomography, Corros. Sci. 58 (2012) 299–306. https://doi.org/10.1016/j.corsci.2012.02.001.

[9] F.M. Queiroz, M. Terada, A.F.S. Bugarin, H.G. de Melo, I. Costa, Comparison of Corrosion Resistance of the AA2524-T3 and the AA2024-T3, Metals (Basel). 11 (2021) 980. https://doi.org/10.3390/met11060980.

[10] P. Kwolek, Corrosion behaviour of 7075 aluminium alloy in acidic solution, RSC Adv. 10 (2020) 26078–26089. https://doi.org/10.1039/d0ra04215c.

[11] V.R. Capelossi, M. Poelman, I. Recloux, R.P.B. Hernandez, H.G. De Melo, M.G. Olivier, Corrosion protection of clad 2024 aluminum alloy anodized in tartaric-sulfuric acid bath and protected with hybrid sol-gel coating, Electrochim. Acta. 124 (2014) 69–79. https://doi.org/10.1016/j.electacta.2013.09.004.

[12] G. Boisier, N. Pébère, C. Druez, M. Villatte, S. Suel, FESEM and EIS Study of Sealed AA2024 T3 Anodized in Sulfuric Acid Electrolytes: Influence of Tartaric Acid, J. Electrochem. Soc. 155 (2008) C521. https://doi.org/10.1149/1.2969277.

[13] W. Lee, S.-J. Park, Porous Anodic Aluminum Oxide: Anodization and Templated Synthesis of Functional Nanostructures, Chem. Rev. 114 (2014) 7487–7556. https://doi.org/10.1021/cr500002z.

[14] G.E. Thompson, H. Habazaki, K. Shimizu, M. Sakairi, G.C. Wood, Anodizing of aluminium alloys, Aircr. Eng. Aerosp. Technol. 71 (1999) 228–238.

[15] F. Mansfeld, Evaluation of Anodized Aluminum Surfaces with Electrochemical Impedance Spectroscopy, J. Electrochem. Soc. 135 (1988) 828. https://doi.org/10.1149/1.2095786.

[16] O.M. Prada Ramirez, F.M. Queiroz, M.A. Tunes, R.A. Antunes, C.L. Rodrigues, A. Lanzutti, S. Pogatscher, M. Olivier, H.G. De Melo, Tartaric-sulphuric acid anodized clad AA2024-T3 post-treated in Ce-containing solutions at different temperatures: Corrosion behaviour and Ce ions distribution, Appl. Surf. Sci. 534 (2020) 147634. https://doi.org/10.1016/j.apsusc.2020.147634.

[17] F.C.G. Rueda, J.T. González, J.M. Hernández-López, Differences between the untreated and treated diffusion zone in the Alclad 2024-T3 aluminum alloy and hard anodic films, Surf. Coatings Technol. (2021) 127939. https://doi.org/10.1016/j.surfcoat.2021.127939.

[18] T. Song, Q. Liu, M. Zhang, R. Chen, K. Takahashi, X. Jing, L. Liu, J. Wang, Multiple sheet-layered super slippery surfaces based on anodic aluminium oxide and its anticorrosion property, RSC Adv. 5 (2015) 70080–70085. https://doi.org/10.1039/c5ra11263j.

[19] A. Ruiz-Clavijo, O. Caballero-Calero, M. Martín-González, Revisiting anodic alumina templates: From fabrication to applications, Nanoscale. 13 (2021) 2227–2265. https://doi.org/10.1039/d0nr07582e.

[20] M. Curioni, M. Saenz de Miera, P. Skeldon, G.E. Thompson, J. Ferguson, Macroscopic

and Local Filming Behavior of AA2024 T3 Aluminum Alloy during Anodizing in Sulfuric Acid Electrolyte, J. Electrochem. Soc. 155 (2008) C387. https://doi.org/10.1149/1.2931522.

[21] Y. Ma, X. Zhou, G.E. Thompson, M. Curioni, T. Hashimoto, P. Skeldon, P. Thomson, M. Fowles, Anodic Film Formation on AA 2099-T8 Aluminum Alloy in Tartaric–Sulfuric Acid, J. Electrochem. Soc. 158 (2011) C17. https://doi.org/10.1149/1.3523262.

[22] L.E. Fratila-Apachitei, J. Duszczyk, L. Katgerman, Voltage transients and morphology of AlSi(Cu) anodic oxide layers formed in H2SO4 at low temperature, Surf. Coatings Technol. 157 (2002) 80–94. https://doi.org/10.1016/S0257-8972(02)00144-5.

[23] Y. Ma, X. Zhou, G.E. Thompson, M. Curioni, X. Zhong, E. Koroleva, P. Skeldon, P. Thomson, M. Fowles, Discontinuities in the porous anodic film formed on AA2099-T8 aluminium alloy, Corros. Sci. 53 (2011) 4141–4151. https://doi.org/10.1016/j.corsci.2011.08.023.

[24] Y. Sen Huang, T.S. Shih, J.H. Chou, Electrochemical behavior of anodized AA7075-T73 alloys as affected by the matrix structure, Appl. Surf. Sci. 283 (2013) 249–257. https://doi.org/10.1016/j.apsusc.2013.06.094.

[25] A. Doublet, M. Kjellberg, B. Jousselme, M. Pinault, G. Deniau, R. Cornut, G. Charrier, Bifunctional coatings: Coupling an organic adhesion promoter with an anticorrosion inorganic layer, RSC Adv. 9 (2019) 24043–24049. https://doi.org/10.1039/c9ra03657a.

[26] M. García-Rubio, M.P. de Lara, P. Ocón, S. Diekhoff, M. Beneke, A. Lavía, I. García, Effect of postreatment on the corrosion behaviour of tartaric-sulphuric anodic films, Electrochim. Acta. 54 (2009) 4789–4800. https://doi.org/10.1016/j.electacta.2009.03.083.

[27] S.T. Abrahami, Cr(VI)-free pre-treatments for adhesive bonding of aerospace industry, TU Delft, 2016.

[28] M. Kendig, S. Jeanjaquet, R. Addison, J. Waldrop, Role of hexavalent chromium in the inhibition of corrosion of aluminum alloys, Surf. Coatings Technol. 140 (2001) 58–66. https://doi.org/10.1016/S0257-8972(01)01099-4.

[29] A. Carangelo, M. Curioni, A. Acquesta, T. Monetta, F. Bellucci, Application of EIS to In Situ Characterization of Hydrothermal Sealing of Anodized Aluminum Alloys: Comparison between Hexavalent Chromium-Based Sealing, Hot Water Sealing and Cerium-Based Sealing, J. Electrochem. Soc. 163 (2016) C619–C626. https://doi.org/10.1149/2.0231610jes.

[30] P. Visser, Y. Liu, X. Zhou, T. Hashimoto, G.E. Thompson, S.B. Lyon, L.G.J. Van Der Ven, A.J.M.C. Mol, H.A. Terryn, The corrosion protection of AA2024-T3 aluminium alloy by leaching of lithium-containing salts from organic coatings, Faraday Discuss. 180 (2015) 511–526. https://doi.org/10.1039/c4fd00237g.

[31] (Occupational Safety and HealthAdministration) OSHA, Hexavalent Chromium, (2009) OSHA 3373-10 (2009).

[32] REACH (Registration, Evaluation, Authorisation and Restriction of Chemicals); REACH Annex XVII: REACH Restricted Substance List (2019), (2019).

[33] BOEING, BAC 5632 Boric Acid - Sulfuric Acid Anodizing, (2004) Revision D.

[34] H. Costenaro, A. Lanzutti, Y. Paint, L. Fedrizzi, M. Terada, H.G. de Melo, M.G. Olivier, Corrosion resistance of 2524 Al alloy anodized in tartaric-sulphuric acid at different voltages and protected with a TEOS-GPTMS hybrid sol-gel coating, Surf. Coatings Technol. (2017). https://doi.org/10.1016/j.surfcoat.2017.05.090.

[35] S.T. Abrahami, J.M.M. de Kok, H. Terryn, J.M.C. Mol, Towards Cr(VI)-free anodization of aluminum alloys for aerospace adhesive bonding applications: A review, Front. Chem. Sci. Eng. 11 (2017) 465–482. https://doi.org/10.1007/s11705-017-1641-3.

[36] B. WILSON, L.; HINTON, A Method of Forming a Corrosion Resistant Coating, Australian Patent WO 88/06639, (1988).

[37] L. Armelao, M. Dabalà, I. Calliari, A. Buchberger, Cerium-based conversion layers on aluminum alloys, Appl. Surf. Sci. 172 (2001) 312–322. https://doi.org/10.1016/S0169-4332(00)00873-4.

[38] L.E.M. Palomino, J.F.W. De Castro, I. V. Aoki, H.G. De Melo, Microstructural and electrochemical characterization of environmentally friendly conversion layers on aluminium alloys, J. Braz. Chem. Soc. 14 (2003) 651–659. https://doi.org/10.1590/S0103-50532003000400024.

[39] J.H.W. de W. P. Campestrini , H. Terryn, A. Hovestad, Formation of a cerium-based conversion coating on AA2024: relationship with the microstructure, Surf. Coatings Technol. 176 (2003) 365–381. https://doi.org/10.1016/S0257-8972.

[40] D. Lau, A.M. Glenn, A.E. Hughes, F.H. Scholes, T.H. Muster, S.G. Hardin, Factors influencing the deposition of Ce-based conversion coatings, Part II: The role of localised reactions, Surf. Coatings Technol. 203 (2009) 2937–2945. https://doi.org/10.1016/j.surfcoat.2009.03.016.

[41] A.E. Hughes, F.H. Scholes, A.M. Glenn, D. Lau, T.H. Muster, S.G. Hardin, Factors influencing the deposition of Ce-based conversion coatings, part I: The role of Al3+ ions, Surf. Coatings Technol. 203 (2009) 2927–2936. https://doi.org/10.1016/j.surfcoat.2009.03.022.

[42] B.R.W. Hinton, D.R. Arnott, N.E. Ryan, Inhibition of Aluminum Alloy Corrosion By Cerous Cations., Met. Forum. 7 (1984) 211–217.

[43] D.R. Arnott, N.E. Ryan, B.R.W. Hinton, B.A. Sexton, A.E. Hughes, Auger and XPS studies of cerium corrosion inhibition on 7075 aluminum alloy, Appl. Surf. Sci. 22–23 (1985) 236–251. https://doi.org/10.1016/0378-5963(85)90056-X.

[44] B.R.W. Hinton, Corrosion inhibition with rare earth metal salts, J. Alloys Compd. 180 (1992) 15–25. https://doi.org/10.1016/0925-8388(92)90359-H.

[45] F.H. Scholes, C. Soste, A.E. Hughes, S.G. Hardin, P.R. Curtis, The role of hydrogen peroxide in the deposition of cerium-based conversion coatings, Appl. Surf. Sci. 253 (2006) 1770–1780. https://doi.org/10.1016/j.apsusc.2006.03.010.

[46] A. Decroly, J.P. Petitjean, Study of the deposition of cerium oxide by conversion on to aluminium alloys, Surf. Coatings Technol. 194 (2005) 1–9. https://doi.org/10.1016/j.surfcoat.2004.05.012.

[47] I. V. Gordovskaya, T. Hashimoto, J. Walton, M. Curioni, G.E. Thompson, P. Skeldon, Development of Cerium-Rich Layers on Anodic Films Formed on Pure Aluminium

and AA7075 T6 Alloy, J. Electrochem. Soc. 161 (2014) C601–C606. https://doi.org/10.1149/2.0091501jes.

[48] P. Yu, S.A. Hayes, T.J.O. Keefe, M.J.O. Keefe, J.O. Stoffer, The Phase Stability of Cerium Species in Aqueous Systems and Pourbaix Diagram Calculations, (2006) 74–79. https://doi.org/10.1149/1.2130572.

[49] M. Saeedikhani, M. Javidi, S. Vafakhah, Anodising of 2024-T3 aluminium alloy in electrolyte of sulphuric– boric–phosphoric mixed acid containing cerium salt as corrosion inhibitor, Trans. Nonferrous Met. Soc. China (English Ed. 27 (2017) 711–721. https://doi.org/10.1016/S1003-6326(17)60079-7.

[50] A. Carangelo, M. Curioni, A. Acquesta, T. Monetta, F. Bellucci, Cerium-Based Sealing of Anodic Films on AA2024T3: Effect of Pore Morphology on Anticorrosion Performance, J. Electrochem. Soc. 163 (2016) C907–C916. https://doi.org/10.1149/2.1001614jes.

[51] M. Terada, F.M. Queiroz, D.B.S. Aguiar, V.H. Ayusso, H. Costenaro, M.-G. Olivier, H.G. de Melo, I. Costa, Corrosion resistance of tartaric-sulfuric acid anodized AA2024-T3 sealed with Ce and protected with hybrid sol–gel coating, Surf. Coatings Technol. (2019). https://doi.org/10.1016/j.surfcoat.2019.05.028.

[52] O.M. Prada Ramirez, F.M. Queiroz, M. Terada, U. Donatus, I. Costa, M.G. Olivier, H.G. de Melo, EIS investigation of a Ce-based posttreatment step on the corrosion behaviour of Alclad AA2024 anodized in TSA, Surf. Interface Anal. 51 (2019) 1260–1275. https://doi.org/10.1002/sia.6633.

[53] The Aluminium Association, International Alloy Designations and Chemical Composition Limits for Wrought Aluminum and Wrought Aluminum Alloys With Support for On-line Access From: Aluminum Extruders Council Use of the Information, Alum. Assoc. Arlington, Virginia. (2015) 31. https://www.aluminum.org/sites/default/files/Teal Sheets.pdf.

[54] H. Costenaro, F.M. Queiroz, M. Terada, M.G. Olivier, I. Costa, H.G. De Melo, Corrosion Protection of AA2524-T3 Anodized in Tartaric-Sulfuric Acid Bath and Protected with Hybrid Sol-Gel Coating, Key Eng. Mater. 710 (2016) 210–215. https://doi.org/10.4028/www.scientific.net/KEM.710.210.

[55] L.A. Giannuzzi, F.A. Stevie, A review of focused ion beam milling techniques for TEM specimen preparation, Micron. 30 (1999) 197–204. https://doi.org/10.1016/S0968-4328(99)00005-0.

[56] P. Eaton, P. Quaresma, C. Soares, C. Neves, M.P. de Almeida, E. Pereira, P. West, A direct comparison of experimental methods to measure dimensions of synthetic nanoparticles, Ultramicroscopy. 182 (2017) 179–190. https://doi.org/10.1016/j.ultramic.2017.07.001.

[57] P. Eaton, P. West, Atomic Force Microscopy, Oxford University Press, Oxford, 2010.

[58] M. Saenz De Miera, M. Curioni, P. Skeldon, G.E. Thompson, Preferential anodic oxidation of second-phase constituents during anodising of AA2024-T3 and AA7075-T6 alloys, Surf. Interface Anal. 42 (2010) 241–246. https://doi.org/10.1002/sia.3191.

[59] Y. Ma, H. Wu, X. Zhou, K. Li, Y. Liao, Z. Liang, L. Liu, Corrosion behavior of anodized Al-Cu-Li alloy: The role of intermetallic particle-introduced film defects,

Corros. Sci. 158 (2019). https://doi.org/10.1016/j.corsci.2019.108110.

[60] H. Wu, Y. Ma, W. Huang, X. Zhou, K. Li, Y. Liao, Z. Wang, Z. Liang, L. Liu, Effect of Iron-Containing Intermetallic Particles on Film Structure and Corrosion Resistance of Anodized AA2099 Alloy, J. Electrochem. Soc. 165 (2018) C573–C581. https://doi.org/10.1149/2.1361809jes.

[61] D. Veys-Renaux, N. Chahboun, E. Rocca, Anodizing of multiphase aluminium alloys in sulfuric acid: in-situ electrochemical behaviour and oxide properties, Electrochim. Acta. 211 (2016) 1056–1065. https://doi.org/10.1016/j.electacta.2016.06.131.

[62] M. García-Rubio, P. Ocón, A. Climent-Font, R.W. Smith, M. Curioni, G.E. Thompson, P. Skeldon, A. Lavía, I. García, Influence of molybdate species on the tartaric acid/sulphuric acid anodic films grown on AA2024 T3 aerospace alloy, Corros. Sci. (2009). https://doi.org/10.1016/j.corsci.2009.05.034.

[63] O.M.P. Ramirez, Estudo da resistência à corrosão da liga de alumínio 2024-T3 clad anodizada em ácido tartárico sulfúrico e pós-tratada em banho contendo íons Ce., Universidade de São Paulo, 2019. https://doi.org/10.11606/D.3.2019.tde-16092019-091627.

[64] Ceric ammonium nitrate, Wikipedia. (2022). https://en.wikipedia.org/wiki/Ceric_ammonium_nitrate (accessed April 9, 2022).

[65] F.M. Queiroz, M. Magnani, I. Costa, H.G. de Melo, Investigation of the corrosion behaviour of AA 2024-T3 in low concentrated chloride media, Corros. Sci. 50 (2008) 2646–2657. https://doi.org/10.1016/j.corsci.2008.06.041.

[66] A. Boag, A.E. Hughes, A.M. Glenn, T.H. Muster, D. McCulloch, Corrosion of AA2024-T3 Part I: Localised corrosion of isolated IM particles, Corros. Sci. 53 (2011) 17–26. https://doi.org/10.1016/j.corsci.2010.09.009.

[67] A.E. Hughes, R. Parvizi, M. Forsyth, Microstructure and corrosion of AA2024, Corros. Rev. 33 (2015) 1–30. https://doi.org/10.1515/corrrev-2014-0039.

[68] M.A. Arenas, A. Conde, J.J. De Damborenea, Effect of acid traces on hydrothermal sealing of anodising layers on 2024 aluminium alloy, Electrochim. Acta. 55 (2010) 8704–8708. https://doi.org/10.1016/j.electacta.2010.07.089.

[69] X. hui Zhao, Y. Zuo, J. mao Zhao, J. ping Xiong, Y. ming Tang, A study on the self-sealing process of anodic films on aluminum by EIS, Surf. Coatings Technol. 200 (2006) 6846–6853. https://doi.org/10.1016/j.surfcoat.2005.10.031.

[70] B. Hirschorn, M.E. Orazem, B. Tribollet, V. Vivier, I. Frateur, M. Musiani, Constant-Phase-Element Behavior Caused by Coupled Resistivity and Permittivity Distributions in Films, J. Electrochem. Soc. 158 (2011) C424. https://doi.org/10.1149/2.039112jes.

[71] M. Saeedikhani, M. Javidi, A. Yazdani, Anodizing of 2024-T3 aluminum alloy in sulfuric-boric-phosphoric acids and its corrosion behavior, Trans. Nonferrous Met. Soc. China (English Ed. 23 (2013) 2551–2559. https://doi.org/10.1016/S1003-6326(13)62767-3.

[72] R. del Olmo, U. Tiringer, I. Milošev, P. Visser, R. Arrabal, E. Matykina, J.M.C. Mol, Hybrid sol-gel coatings applied on anodized AA2024-T3 for active corrosion protection, Surf. Coat. Technol. (2021) 142972. https://doi.org/10.1016/j.surfcoat.2021.127251.

[73] M. García-Rubio, P. Ocón, M. Curioni, G.E. Thompson, P. Skeldon, A. Lavía, I. García, Degradation of the corrosion resistance of anodic oxide films through immersion in the anodising electrolyte, Corros. Sci. 52 (2010) 2219–2227. https://doi.org/10.1016/j.corsci.2010.03.004.

[74] Y. Ma, X. Zhou, W. Huang, G.E. Thompson, X. Zhang, C. Luo, Z. Sun, Localized corrosion in AA2099-T83 aluminum-lithium alloy: The role of intermetallic particles, Mater. Chem. Phys. 161 (2015) 201–210. https://doi.org/10.1016/j.matchemphys.2015.05.037.

[75] A.M. Glenn, T.H. Muster, C. Luo, X. Zhou, G.E. Thompson, A. Boag, A.E. Hughes, Corrosion of AA2024-T3 Part III: Propagation, Corros. Sci. 53 (2011) 40–50. https://doi.org/10.1016/j.corsci.2010.09.035.

[76] M. Aggerbeck, S. Canulescu, K. Dirscherl, V.E. Johansen, S. Engberg, J. Schou, R. Ambat, Appearance of anodised aluminium: Effect of alloy composition and prior surface finish, Surf. Coatings Technol. 254 (2014) 28–41. https://doi.org/10.1016/j.surfcoat.2014.05.047.

[77] M. Curioni, P. Skeldon, E. Koroleva, G.E. Thompson, J. Ferguson, Role of Tartaric Acid on the Anodizing and Corrosion Behavior of AA 2024 T3 Aluminum Alloy, J. Electrochem. Soc. (2009). https://doi.org/10.1149/1.3077602.

[78] R. del Olmo, M. Mohedano, P. Visser, A. Rodriguez, E. Matykina, R. Arrabal, Effect of cerium (IV) on thin sulfuric acid anodizing of 2024-T3 alloy, J. Mater. Res. Technol. 15 (2021) 3240–3254. https://doi.org/10.1016/j.jmrt.2021.09.117.

[79] J.M. Torrescano-Alvarez, M. Curioni, P. Skeldon, Effects of oxygen evolution on the voltage and film morphology during galvanostatic anodizing of AA 2024-T3 aluminium alloy in sulphuric acid at −2 and 24 °C, Electrochim. Acta. 275 (2018) 172–181. https://doi.org/10.1016/j.electacta.2018.03.121.

[80] Y.D. Li, Y. Zhang, S.M. Li, P.Z. Zhao, Influence of adipic acid on anodic film formation and corrosion resistance of 2024 aluminum alloy, Trans. Nonferrous Met. Soc. China (English Ed. 26 (2016) 492–500. https://doi.org/10.1016/S1003-6326(16)64137-7.

[81] J. Xu, G. Li, L. Li, CeO2 nanocrystals: Seed-mediated synthesis and size control, Mater. Res. Bull. 43 (2008) 990–995. https://doi.org/10.1016/j.materresbull.2007.04.019.

[82] Z. Bao, K. Li, S. Wang, K. Gao, D. Zhang, M. Li, Preparation and characterization of submicron-cerium oxide by hypergravity coprecipitation method, Adv. Powder Technol. 32 (2021) 1611–1618. https://doi.org/10.1016/j.apt.2021.03.016.

CRediT authorship contribution statement

Oscar Mauricio Prada Ramirez: Investigation, Visualization, Writing – Original Draft. **Matheus Araujo Tunes:** Formal analysis, Visualization, Writing – Review & editing. **Marina Martins Mennucci:** Conceptualization, Writing – Review & editing. **Maksim Starykevich:** Formal analysis, Visualization, Writing – Review & editing. **Cristina Neves:** Formal analysis, Visualization, Writing – Review & editing. **Mário G. S. Ferreira:** Validation, Writing – Review & editing. **Stefan Pogatscher:** Validation, Writing – Review &

editing. **Hercílio Gomes De Melo:** Project administration, Supervision, Writing – Review & editing.

Declaration of Competing Interest

☒ The authors declare that they have no known competing financial interests or personal relationships that could have appeared to influence the work reported in this paper.

☐The authors declare the following financial interests/personal relationships which may be considered as potential competing interests:

Graphical abstract

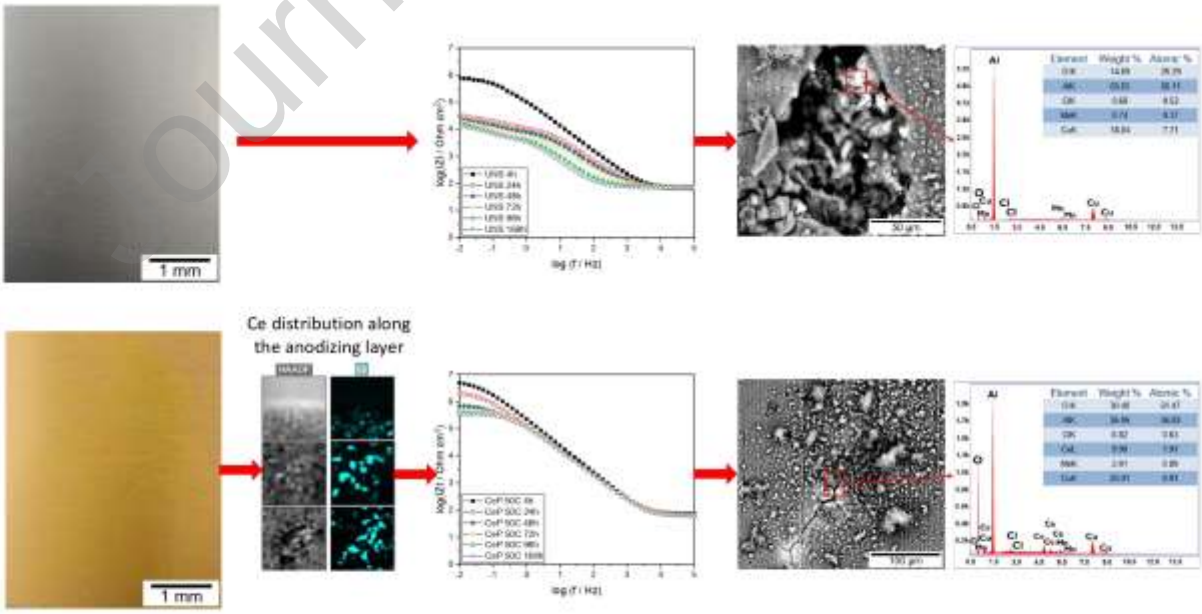

Highlights

- The post-treatment increases the corrosion resistance of the anodic layer.

- The pores of the anodic layer remain open.
- The deposition of Ce nanoparticles within the pores of the anodic layer has been demonstrated.
- Evidences that Ce ions durably remains in the layer hindering corrosion activity.